IN-SITU 3D PRINTED BIOSILICATE NANOPARTICLE-BASED SCAFFOLDS FOR RAPID BONE DEFECT HEALING

A Thesis

by

TAHA AZIMAIE

Submitted to the Office of Graduate and Professional Studies of
Texas A&M University
in partial fulfillment of the requirements for the degree of

MASTER OF SCIENCE

Chair of Committee,	Venu Varanasi
Co-Chair of Committee	Phillip Kramer
Committee Members,	Lynne Opperman
	Peter Buschang
Head of Department,	Larry Bellinger

December 2016

Major Subject: Oral Biology

ABSTRACT

Craniofacial reconstruction surgeries are extremely challenging because of the complex anatomy of the region and its proximity to the vital tissues. These surgeries usually require custom implants. Fabrication of a custom implant is time consuming and delay the surgery which increase the risk of a successful operation. Therefore, a new surgical method is needed to treat bone defects with the least possible delay, and without compromising precision in fabrication and implantation. This study introduces in-situ printing (ISP) as a solution; by directly printing scaffolds into defects of patients, ISP can combine fabrication and implantation of micropatterned scaffolds and possibly eliminate fabrication delay, improve implantation precision and provide a capacity to modify the scaffold's shape during surgery. This study consists of two main parts: the first optimizes a methacrylated gelatin (MAG), Laponite (LP) nanocomposite as a material for ISP and the other tests physical properties of the nanocomposite.

To optimize MAG, sucrose was added to the nanocomposite to reduce gelation and increase printability. Printing parameters including UV intensity for crosslinking MAG, extrusion rate, and printing speed were modified for the purpose of ISP. A critical sized calvarial defect in rat models were treated by ISP using the modified nanocomposite. Four weeks after the surgery, the treated region was characterized using SEM, EDS, μCT, Raman, and histological analysis. Results showed that more than 50% of the ISP treated defect was healed in 4 weeks with no inflammation or infection. The healed region were chemically and histologically similar to rat's native bone.

Study on physical properties of nanocomposite revealed that increasing LP concentration from 0 to 6 %wt. reduced hydrolytic degradation, swelling, and protein release rates, while increasing MAG from 10 to 20 %wt. reduced enzymatic degradation, and increased swelling and protein release rates.

These findings suggest that ISP of MAG-LP nanocomposites can be used for bone defect treatment without introducing any complication and also physical properties of the nanocomposite can be modified by adjusting MAG and LP concentrations.

To the loving memory of my mother…

And to

Her…

ACKNOWLEDGEMENTS

I would like to take this opportunity to express my appreciation and thanks to my committee chair, Dr. Venu Varanasi, and my committee members, Regent Professor Lynne Opperman, Regent Professor Peter Buschang, and Professor Philip Kramer, for reviewing this dissertation and being so giving with their time and input.

I'd like especially to thank Dr. Xiaohua Liu and members of his lab Dr. Chi Ma and Dr. Xiaogang Cheng for sharing their facilities and opinions with me.

I also want to extend my gratitude to Dr. Phillipe Monte, Tugba Cebe, and Annabelle Yao from Dr. Aswath's lab for assisting me through my thesis and also Characterization Center for Materials and Biology at University of Texas at Arlington for providing me the opportunity to use their facilities.

For generously offering human cells for this thesis I would like to acknowledge Dr. Harry Kim from Texas Scottish Rite Hospital for Children.

A big thanks goes to all past and present post-docs and volunteers in our lab Dr. Neda Saffarian, Dr. Azhar Alias, Ross Grounds, and Shadi Zamani for their help, support, and also fun time we had together.

A special thanks to Regent Professor Kathy Svoboda, the director of Oral Biology graduate program, for patiently tolerating my crazy adventurous self.

Thanks also go to my friends, colleagues, faculty, and staff in the Department of Biomedical Sciences for making my time at Texas A&M University a great experience.

NOMENCLATURE

0-10	A bio-ink of 0% LP, 10% MAG, 2% Suc, and 0.05% I2959
2-10	A bio-ink of 2% LP, 10% MAG, 2% Suc, and 0.05% I2959
2D	Two Dimensional
3D	Three Dimensional
3DP	3-Dimensional Printing
4-10	A bio-ink of 4% LP, 10% MAG, 2% Suc, and 0.05% I2959
6-10	A bio-ink of 6% LP, 10% MAG, 2% Suc, and 0.05% I2959
6-15	A bio-ink of 6% LP, 15% MAG, 3% Suc, and 0.075% I2959
6-20	A bio-ink of 6% LP, 20% MAG, 4% Suc, and 0.1% I2959
α-MEM	Alpha modified Minimum Essential Media
μCT	Micro Computed tomography
ACGIH	American Conference of Governmental Industrial Hygienists
ARP	Additive Rapid Prototyping
BMP	Bone Morphogenetic Protein
bpm	Beats Per Minute
BSA	Bovine Serum Albumin
BSE	Back-Scattered Electron microscopy
Ca	Calcium
CAD	Computer Aided Design
CAM	Computer Aided Manufacturing

CSD	Critical Size Defects
CT	Computed tomography
DAPI	4',6-Diamideino-2-Phenylindole
DMF	Dimethylformamide
DPBS	Dulbecco’s Phosphate Buffered Saline
ECM	Extra Cellular Matrix
EDS	Energy-Dispersive X-ray Spectroscopy
EtO	Ethylene Oxide
EtOH	Ethanol
FBS	Fetal Bovine Serum
FGF	Fibroblast Growth Factors
FITC-BSA	Fluorescein isothiocyanate conjugated bovine serum albumin
FTIR	Fourier Transform Infrared Spectroscopy
GPS	Global Positioning System
H&E	Hematoxylin and Eosin
HA	HydroxyApatite
I2959	IRGACURE2959
IACUC	Institutional Animal Care and Use Committee
ICP-OES	Inductively coupled plasma optical emission spectrometry
IR	Infrared electromagnetic wave
IRB	Institutional Review Board
ISP	In-Situ Printing

Krpm	Kilo Revolutions Per Minute
LP	Laponite
MA	Methacrylate Anhydride
MAG	Methacrylated Gelatin
MI	Mineral isle
MRI	Magnetic Resonance Imaging
NH_3	Amino chemical group
O	Oxygen
OH	Hydroxyl chemical group
P	Phosphorous
PBS	Phosphate Buffered Saline
PCL	Poly Caprolactone
PDPC	Periosteum Derived Progenitor Cells
PEG	Poly Ethylene Glycol
PII	Prosthetic Implant Infection
PLA	Poly Lactic Acid
PGA	Poly Glycolic Acid
PLGA	Poly Lactic-co-Glycolic Acid
RB	Regenerated Bone
RGD	Arginylglycylaspartic acid
RMF	Re-Mineralization Front
RP	Rapid Prototyping

rpm	Revolution Per Minute
RUNX2	Runt-related Transcription Factor 2
SB	Surrounding Bone (indigenous rat bone)
SEI	Secondry Electron Imaging
SEM	Scanning Electron Microscopy imaging
Si^{+4}	Silicon ion with a charge of +4
Suc	Sucrose
TCP	Tri-Calcium Phosphate
THF	Tetrahydrofuran
UV	Ultra Violet light
VEGF	Vascular Endothelial Growth Factor

TABLE OF CONTENTS

Page

Page

Page

LIST OF FIGURES

Page

Page

Page

LIST OF TABLES

Page

CHAPTER I

INTRODUCTION

1.1. History of Tissue Engineering

In the 20th century, the concept of saving and repairing living tissues gained a lot of attention and resulted in the creation of reconstructive surgery. Previously, when tissues became diseased or damaged, saving the life of a patient was the only concern of medicine [1]. Reconstructive surgery was developed as a result of the emergence of aseptic surgery and aimed to enhance the life of a patient by replacing the missing or defective body structure. This replacement could be from many sources: from a part of a patient's own body (autograft), from a different person (allograft), or from an animal (xenograft). Although initially these transplantations were considered successful, new problems have emerged; dislodgment, infection, limited sources, disease transfer, and body rejection were some of the issues. Soon, this area gained considerable attention and the field of tissue engineering was born.

The term "tissue engineering" was coined by Y.C. Fung in 1987 [1]. Since then its definition and aims have evolved radically. Dr. Vacanti defined tissue engineering as "an interdisciplinary field that applies the principles of engineering and the life sciences toward the development of biological substitutes that restore, maintain, or improve tissue formation [2]." As the field expanded, new subfields were created within tissue engineering. To fit newer concepts and developments, National Institute of Health provided a new definition for tissue engineering "Reparative medicine, sometimes

referred to as regenerative medicine or tissue engineering, is the regeneration and remodeling of tissue in vivo for the purpose of repairing, replacing, maintaining, or enhancing organ function, and the engineering and growing of functional tissue substitutes in vitro for implantation in vivo as a biological substitute for damaged or diseased tissues and organs [3].” Although these three terms have similarities, each deviated into a separate field as they developed and became more specialized. Nowadays tissue engineering is defined as the combination of biologically active scaffolds and cells into a functional living tissue [4]. Biologically active materials in this definition are materials that can constructively interact with the biological environment [4]. This thesis is focused on hard tissue engineering. To understand the concept of hard tissue engineering, first, some introductions to the bone healing mechanism and the scaffolds concept are needed.

1.2. Bone Healing Mechanism

Unlike its static appearance, bone is a dynamic tissue which has the ability to heal itself. Bone healing is divided into three steps: an inflammatory phase; a reparative phase, and a remodeling phase [5].

1.2.1. Inflammatory Phase

After bone is damaged, an inflammatory response is triggered which reaches its peak in 48 hours and disappears in a week. This inflammation helps reduce the fracture site movement by inducing pain and hydrostatic swelling [6]. Vascular damage at the wounded site results in bleeding and platelet aggregation. Platelet degranulation results

in growth factor release and activation of the clotting cascade. Hematoma accumulates within the defect and serves as a plug to stop further hemorrhage. Also, the fibrin network in hematoma serves as a scaffold for cell migration to the defect site [7]. Later on, white blood cells are attracted to the site. The hypoxic and acidic environment of the fracture site at the early stage of healing activates macrophages and Polymorphonuclear cells to release cytokines to stimulate angiogenesis [8]. The process of inflammation creates a reparative granuloma which is called an external callus [9].

1.2.2. Reparative Phase

A few days after the trauma and before inflammation disappears, the reparative phase starts. First, osteocytes, periosteum, bone marrow cells, and soft tissue cells around and inside the fracture die from lack of nutrients and are resorbed [10]. At the same time, pluripotent mesenchymal stem cells migrate through blood vessels to the damaged tissue and differentiate into cells such as fibroblasts, chondroblasts, and osteoblasts. These cells form a callus contained fibrous tissue, blood vessels, cartilage, woven bone, and osteoid. Reparative cartilaginous callus forms around and inside the defect and mechanically stabilizes the defect.

During the healing process, two distict mechanism of ossification may occure: endochondral ossification and intramembranous ossification. In endochondral ossification, the pH increases and turns the acidic environment to alkaline. This situation increases the activity of alkaline phosphatase and induces mineralization of the callus [11]. Intramembranous ossification occurs by the differentiation of stem cells directly to osteoblasts that lay down mineral tissue without a cartilaginous step. This occurs in the

external callus and perichondrium and is called hard callus. The calcified callus is weak and only serves to connect the edges of the bone at the fracture site to immobilize them. During the mineralization phase, capillaries begin to invade the callus. After capillaries grow within the hard callus, the remodeling phase starts.

1.2.3. Remodeling Phase

The remodeling phase is similar to normal bone remodeling and consists of dynamic woven bone (hard callus) resorption by osteoclasts and lamellar bone deposition by osteoblasts [12] in response to biomechanical stimulus and hormonal regulation of calcium in the body. Mechanical stresses can trigger the remodeling process in a mechanism not well understood. Calcium level in the serum can stimulate parathyroid hormone secretion. This hormone binds to osteoblast lining cells. These cells, in turn, signal osteoclast precursor cells to fuse and differentiate to multi-nucleated osteoclasts. These multinuclear cells start resorbing minerals in woven bone by secreting hydrochloric acid [13], and collagen matrix by secreting collagenase [14]. Afterwards, osteoblasts are recruited to the surface to form under-mineralized bone (osteoid), which undergoes a mineralization process [15].

1.3. Scaffolds

Scaffolds are 3D structures that mimic the extracellular matrix of human body to mechanically support the defect, facilitate cellular adhesion, migration, and proliferation to promote tissue regeneration. In bone remineralization, scaffolds resemble callus. The ultimate purpose of osteogenic scaffolds are mimicking callus functions to reduce the

time needed for bone healing. Their gross shape usually defines the ultimate shape of the regenerated tissue [16]. To make scaffolds, materials compatible with the biological environment should be used; these materials are called “biomaterials.” Biomaterials can either be harvested from an organism or synthesized. They are characterized by being nontoxic, noncarcinogenic, nonallergic, noninflammatory, biocompatible, and biofunctional for their lifetime [17]. Biomaterials can be divided into three categories: (1) bioinert, (2) bioactive, and (3) bioresorbable [16-18]. Bioinerts are materials that maintain chemical and mechanical stability in the biological environment [18]. Bioactive materials have the ability to chemically bond to living tissue and integrate within them [18]. Bioresorbable materials are gradually absorbed in-vivo and replaced by living tissues.

Biomaterials are included but not limited to bioglass, tri-calcium phosphate (TCP), hydroxyapatite (HA), silicon-based biomaterials and biocompatible polymers, or a combination of these materials [19].

Besides composition, scaffold’s shape and micropatterns also affects scaffold functionality. Figure 1 shows scaffolds with 0.3mm and 0.5mm pore size that robocaster used in this study printed. Also, homogeneity and interconnectivity of pores help to make homogeneous cell distribution and the nutrient circulation that can increase the chance of scaffold integration and faster tissue regeneration [20]. Brock et al reported that when fibroblast cells approach a hollow polygonal shape, they tend to form and stretch lamellipodia at the corners of the polygon and consequently moving toward them [21]. Overall, the direction of cells movement is related to the formation of lamellipodia

and the geometrical shape of the surface affect formation of lamellipodia and as a result, cell migration [22].

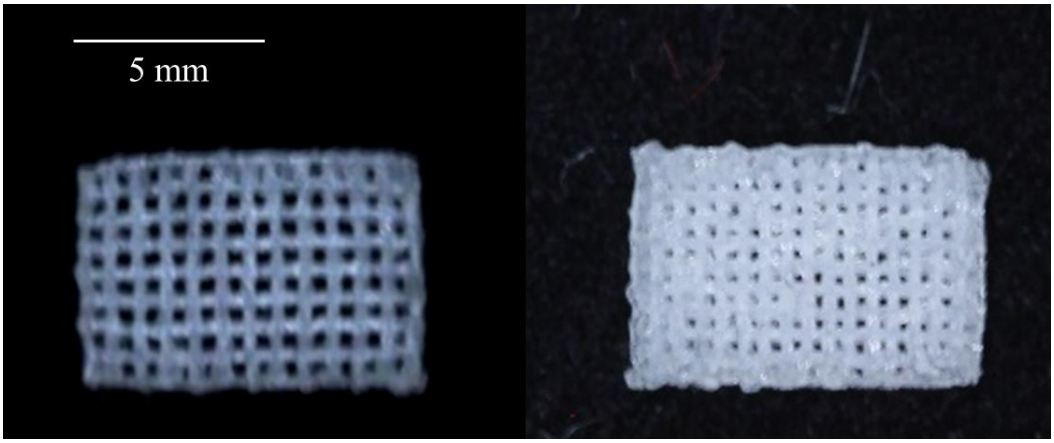

Figure 1. The gross shape of the bio-ink scaffold. The resolution of pores in the scaffold to the right is 0.3 mm. the resolution of pores in the scaffold to the left is 0.5 mm.

Besides pore shape, pore size also plays an important role in cells migration. It is reported that pore size in scaffolds has an optimum that can enhance cell migration the most [23, 24]. If the pore size is too small, cells cannot migrate into pores or stretch their lamellipodia. On the other hand, if the pore size is too big there is not enough surface for cells to adhere and limit cells' attachment. This optimum size differs from one cell type to another [25]. It is been reported that human fetal osteoblasts proliferation on calcium phosphate based materials increases as the pore size decreases from 1mm to 0.5mm [26]. In general, optimum porosity for bone formation and vascularization is reported between 0.3mm to 0.5mm [27-29].

1.4. Clinical Need for Hard Tissue Engineering

Nearly 4,000,000 bone grafting procedures are performed globally every year at a cost of 2.3 billion dollars and it is projected to reach 3.4 billion dollars in 2023 [30]; around 600,000 of these are performed in the US [31]. Bone grafts are used to fill large volumes of bone loss, called critical size defects (CSD), which without grafting or other intervention usually lead to non-union. Bone grafts must have adequate mechanical properties to support new bone formation in the defect and be osteogenic and resorbable to maintain continuity of support during bone regeneration [32]. Currently, allograft, autografts and in some cases xenografts are being used for CSD treatment. However, these materials can cause disease transmission, donor site morbidity, and acute immunological responses that can lead to bone resorption and graft rejection [33]. Also, resources for allografts and autografts are limited. Therefore, there is a vital need for new bone substitutes that can rapidly heal these defects to reduce patient discomfort and medical care costs.

Hard tissue engineering is a broad term that covers many different categories including craniofacial reconstruction surgery, large segmental bone defect reconstruction, spinal fusions, and prosthetic implant fixation. Each category has different challenges and demands. Therefore, the approach for each category could be different, leading to different requirements. This thesis mainly focused on improving craniofacial reconstruction treatment methods. For this purpose, it is required to first identify and recognize advancement and challenges in this field.

1.5. Craniofacial Reconstruction

Annually, thousands of craniofacial reconstructions are performed due to trauma, tumor or congenital deformities such as cleft palate, craniosynostosis, Treacher Collins syndrome, Apert's syndrome, Crouzon's syndrome, hemifacial microsomia and craniofacial skeletal hypoplasias [34]. The gold standard material for this kind of surgeries are autografts and may be taken from a pelvis, ribs, or skull. The healing process for these type of grafting can occur within 3 to 6 months. However, autografts have significant limitations, including donor site morbidity, limited quantities, shape mismatch between the graft and the defect, increased length of surgery, and general anesthesia for harvesting. There is also the addition of titanium implants as a prosthesis or small screws and plates to hold the bones in place. Metal wires also may be used to hold the new bones positions in place [35]. Craniofacial reconstruction also has a huge impact on patient psychological health. The esthetic component of these type of surgeries make them delicate and time consuming; a fraction of millimeter error can compromise the esthetic aspect of the surgery which can have adverse effects on psychosocial life of the patient [36]. Therefore, a highly precise procedure is desired in such surgeries.

1.6. Current Advancements in Craniofacial Reconstruction

Recently, extensive research has been conducted on cells, scaffolds, fabrication, and surgical methods to reduce complications, and improve healing rate.

1.6.1. Surgical Method

Many engineering technologies are being optimized to benefit surgeons by reducing the complexity of craniofacial surgery. Computer aided surgeries are relatively new methods that significantly reduce the complexity of craniofacial surgeries yet increases their precision. Computer aided surgeries can be divided into three main categories: (1) preoperative planning, (2) intraoperative navigation, and (3) intraoperative CT/MRI imaging [37]. Preoperative planning enables the conversion of 2D computed tomography (CT) images to an accurate 3D model. It also enables the clinician to manipulate the virtual model and reconstruct the defect virtually, simulates the surgery, and better design the desired shape of the scaffold. Intraoperative navigation technology is focuses on precise tracking of the position of instruments, the surgical probe, and the surgery site. This technology significantly improved the precision in surgeries. Intraoperative imaging is a technology that helps surgeons to take CT or MRI imaging during surgeries and confirm correct position of implant. This way, surgeons can increase the chance of successful surgery and eliminate the need for a possible second surgery.

1.6.2. Rapid Prototyping

The shape and dimensions of a scaffold are critical for increasing the chance of a successful surgery. Conventional methods that are being used for fabrication of 3D scaffolds are labor-intensive, time-consuming, and do not provide precise control over the scaffold's architecture. Rapid prototyping (RP) is a technique that has revolutionized the fabrication industry. This technology has also successfully made its way into

medicine and has make a significant impact on the field of medical prostheses. Rapid prototyping can be divided into the additive and subtractive method. Additive rapid prototyping (ARP) is more popular because of its ability to create further complex shapes and hollow structures. Today ARP is being increasingly used for tissue engineering [38] and craniofacial reconstruction [37]. Currently in craniofacial reconstruction, APR technology is used for preoperative treatment planning by fabricating a 3D shape of the site of surgery and practicing the surgery on the model [37].

ARP is a broad category that includes many different methods including stereolithography, fused deposition modeling, direct metal laser sintering, laminated object manufacturing, electron beam melting, selective laser sintering, laser engineered net shaping, and 3-dimensional printing (3DP). 3DP does not require heat for its functionality which makes it useful for cell or growth factor incorporation. This feature made 3DP an attractive method for tissue engineering [39]. Robocasting or direct ink writing (DIW) is a subcategory of 3DP that is based on a computer aided fabrication method that uses extrusion of the “ink” while moving in all three axes to make a 2D layer. By adding these 2D layers on top of each other, a 3D object can be created. The robocaster allows precise control of micropatterning by determining the dimensions of filaments, the size and shape of pores and the percentage of porosity of the scaffold [40-42]. Although extensive research has been conducted on suitable biomaterials for 3DP, there are few well-stablished biomaterials on the market that can be 3D printed and

implanted in the body [42]. These materials include bioceramics such as bioglass, TCP, and HA, and biopolymers such as PLA, PGA, and PLGA.

1.7. Current Challenges in Craniofacial Surgical Methodology

Craniofacial reconstruction is a sophisticated surgery that could be challenging for highly skilled surgeons even with all advancement in the surgical methodology. Anatomical complexity of the region, sensitivity and vitality of tissues around the defect and a high chance of infection are some of the reasons these operations are complicated. Currently, autograft is the gold standard for craniofacial reconstruction. These grafts have many limitations including site morbidity, an increase in the operation's complexity, a lack of precision in shape and implantation, limited availability, extra surgeries, additional discomfort for the patient, and an increased chance of infection in donor and recipient site. Synthetic implants are also being used in routine procedures. Most of synthetic scaffolds for this region have custom shapes. The lengthy process of custom shaped implant fabrication usually delays the scaffold implantation which will reduce the chance of healing [43] and possibly can increase mortality rates.

Although 3D printed custom implants have great advantages over other methods of implant fabrication, they cannot solve some common challenges in craniofacial bone grafting including implant loosening and infection [44]. Prosthetic implant infection (PII) is a common infection that mostly happens post-operatively [45]. To prevent infection, handling and transferring pre-fabricated implants should be done in sterile condition. All these processes are labor intensive and cannot completely eliminate the

chance of contamination. Also, most of the materials used for 3D printing require post-fabrication modifications like sintering, and surface chemical and/or physical modification which are time consuming and delays the surgery.

After implantation, the scaffold should "integrate" with the surrounding tissue. The integration has two steps: Bony union and graft remodeling [46]. Bony union occurs at surfaces of the implant in contact with native bone segments. To facilitate bony union, scaffolds needed to almost perfectly fit in the recipient site [47]. Since defect shape after dissection and/or preparation may not perfectly matches the custom made scaffold, cell migration onto the scaffold will be slowed down and consequently delay or interrupt the bony union phase. Therefore, a surgical methodology is required that reduce the mismatch between the defect and the scaffold. This methodology can be based on preparing the defect shape precisely according to the scaffold's shape or be based on fabricating the scaffold after preparing the defect and during the surgery. The former is time consuming and limits the surgeon's ability to alter the defect intraoperatively. The latter, however, require a fast yet precise method of fabrication that can create an scaffold in a fraction of an hour during the surgery.

Therefore, despite dramatic advancement in this field, surgeries requiring scaffolds are still challenging and there are many problems to solve before new craniofacial surgery methods or optimized current ones can be implemented.

1.8. Current Challenges in Biomaterials

Current advancements in science and technology made it possible to mimic the biological environment and induce healing in the defect, by design and engineering new synthetic biomaterials. Synthetic biomaterials have the potential to substitute natural and biological grafts without the complications usually exhibited by natural bone substitutes (refer to the section 1.4).

1.8.1. Bioceramics

The most common bioceramics available in the market are synthetic Hydroxyapatite (HA) and bioglasses. HA has similar chemistry as biologic HA of bone [48]. They are osteoconductive, facilitate cellular migration, and increase extracellular matrix (ECM) attachment to their matrices. Porous scaffolds made from these materials facilitate mineralized tissue ingress [31, 49]. However, their degradation rate is very slow, and the body cannot resorb them [50].

Si^{4+} contained synthetic biomaterials recently gained much attention. Previous studies [51-54] have shown that leached Si^{4+} from these materials is directly linked to enhancement of collagen type I expression and mineralized tissue synthesis. It also plays a role in enhancing the mechanical properties of bone femurs in mice [55], suggesting that Si^{4+} may play an essential role in influencing matrix physical properties. In mice, rat and chick animal models, Si-deficiency led to the irregular bone development and weak bone formation while administration of elevated dietary levels of Si enhanced bone growth and restored normal bone function [51, 55, 56]. Bioactive glasses are FDA approved Si^{4+} contained biomaterials. They degrade faster than Ca-P based scaffolds and

improve tissue attachment by forming a “bone-like” surface HA layer [57]. These materials, however, degrade partially and microencapsulate within the bone or possibly in the connective tissue. Newly developed mesoporous bioactive glasses would not become microencapsulated. However, in addition to difficulties in the preparation of such scaffolds, they suffer from high degradation rate due to their high surface area. Mesoporous bioactive glass’s fast degradation results in premature resorption and also fast ion release which could lead to ectopic mineralization in connective tissue [58, 59]. Adjusting mesoporous bioactive glass’s degradation rate is challenging due to the lack of control of the porosity in the fabrication process [60, 61].

1.8.2. Biodegradable Polymers

Biodegradable polymers are another category of biomaterials that have application for oral and maxillofacial osseous reconstruction. Although these materials do not have osteogenic properties, their biocompatibility, combined with the ability to reproducibly control their composition, rate of degradation, hydrophobicity / hydrophilicity, and cell attachment has made them attractive materials for investigation. Also, biopolymers can be used for cell, drug, and growth factor delivery [62].

PLA, PGA, and their copolymer, PLGA, are degradable polymers that have been used as resorbable sutures for a long time. The mechanism of degradation is based on hydrolysis and the by-products are glycolic acid and lactic acid. These by-products can later be metabolized by the body [63]. Solvents usually used for PLA, PGA, and their derivatives are chloroform, acetone, DMF, and THF which are all toxic [64]. Therefore, a post-fabrication process usually is required to remove the solvent which is time

consuming and required quality control tests to confirm low concentration of the toxic substances. In recent clinical investigations, these polymers have been used as resorbable bone fixtures where high mechanical stiffness or strength is not required [65-68]. These biopolymers are also suitable for drug delivery applications and could be a vehicle for bone regeneration regulators including BMP, VEGF, FGF, etc [64]. However, synthetic biopolymers of PLA and PGA have relatively few charged groups, compared to natural polymers such as collagen (Gelatin) and chitosan. This is a problem that makes them not suitable for inducing mineralization [69, 70]. The low affinity of cells to attach to the surface of these biopolymers also worsens the problem [71]. To solve this limitation, many investigators have tried to modify the polymer by techniques such as covalent binding of bioactive molecules like RGD motif to PLA and PGA. Although these attempts showed promising results [72, 73], the process of manufacturing the scaffolds is a complex and costly process that makes them impractical at a large industrial scale [5].

Polycaprolactone (PCL) is a highly processable and thermally stable polymer that has many biomedical applications from drug carrier to biodegradable scaffolds. However, its hydrophobic surface and slow degradation (3-4 years) made this polymer less desirable for tissue engineering.

1.8.3. Gelatin Silicate Composites

Gelatin is denatured collagen and is well known for its biocompatibility and biodegradability. Gelatin hydrogels have RGD recognition sequence for cell's integrins receptors that enhances cell attachment to gelatin. Gelatin hydrogel is mechanically too weak and chemically too unstable to be used for biomedical application. Therefore, to

make it stable, it has to be crosslinked [74]. To make gelatin crosslinkable, small crosslinkable molecules should be bound chemically to gelatin's backbone. Chemical and mechanical stability of modified gelatin are determined by the number of grafted crosslinkable molecule on the gelatin's backbone. Also, the degree of crosslinking density can make it possible to modify degradation rate of gelatin.

Crosslinked-gelatin hydrogels possess weak osteogenic properties and also do not have adequate mechanical strength to support the bone defect [75]. However, it is reported that by doping silicate particles in the hydrogel, physical, mechanical and osteogenic characteristics of the hydrogel can be enhanced [76, 77]. Previous studies suggested that laponite (LP) nanopowder can be used as the osteogenic inducer in gelatin matrix [77-81]. LP nano-power ($Na^{+0.7}[(Si_8Mg_{5.5}Li_{0.3})O_{20}(OH)_4]^{-0.7}$) is a silica-based nanoparticle that like bioactive glass, enhance osteogenesis by releasing $Si(OH)_4$. In aqueous environment, LP react with water molecules according to chemical reaction below:

$$Na^{+0.7}[(Si_8Mg_{5.5}Li_{0.3})O_{20}(OH)_4]^{-0.7} + 12H^+ + 8H_2O \rightarrow 0.7Na^+ + 8Si(OH)_4 + 5.5Mg^{2+} + 0.3Li^+$$

This reaction increases alkalinity of the environment by consuming H^+ and also causes leaching of Na^+, Mg^{2+}, and Li^+ ions into the water. Magnesium ion enhances cell adhesion through adhesion proteins of the integrin family [80]. Lithium ion enhances osteogenesis by increasing RUNX2 expression. Li^+ enhances Wnt-associated genes expression that inhibits beta-glycogen synthase kinase-3 which in turn regulates RUNX2 activity [80]. LP particles also have a unique nanodisk shape with the thickness of 1 nm

and an average diameter of 20 nm. This unique shape gives these particles high surface to volume ratio. Also in aqueous environments, LP nanoplatelets gain negative charges due to dissociates of Na^+ from the surface. This negative charge makes the edge the nano-disk particle partially positive relative to the surface. These partial charges cause electrostatic interaction between surfaces and edges of nanoplatelets and eventually induce formation of a homogeneous and transparent hollow nanostructure [82] (Figure 2). This nanostructure increases the solution's viscosity and leads to a thick thixotropic gel in a way that addition of only 2 %wt. LP, significantly increase the viscosity. This phenomenon makes it hard to homogeneously add more LP as increase in LP concentration increase the viscosity [78]. Nanoplatelets of LP can also electrostatically attract charged groups of gelatin polymer chains and create an entangled and rigid structure. Figure 2 shows schematic microstructure of LP and how it interact with gelatin before and after crosslinking.

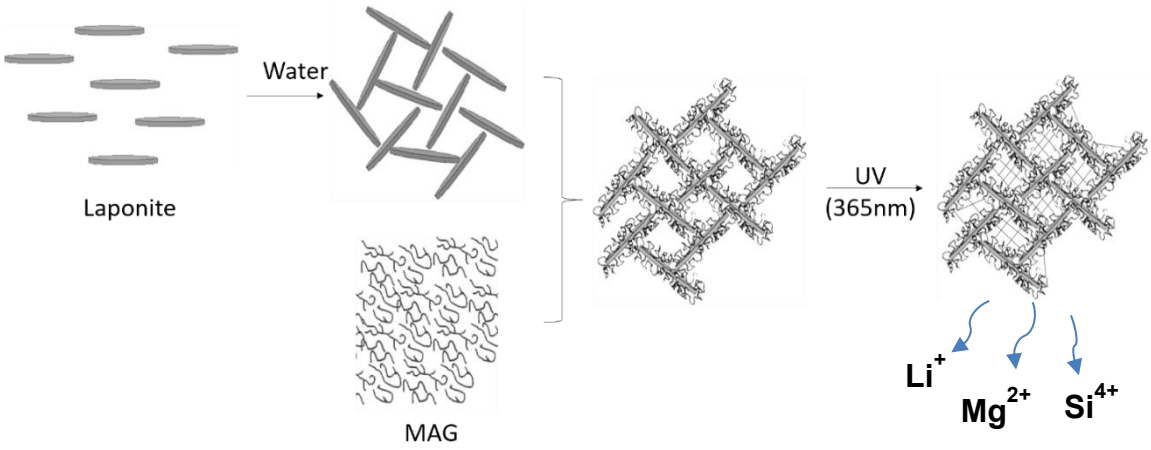

Figure 2. The mixing step to prepare a bio-ink. The final product has a unique entangled network that is formed by ionic interaction between LP and MAG.

All these characteristics make LP a good candidate for enhancing mechanical [79] and osteogenic [80] properties of gelatin-based hydrogel scaffold. However, gelatin hydrogel shapes are highly depend to their hydration level [83]. As a result, keeping their shape intact after fabrication is challenging and expensive. In addition, this composite is fairly new and no in-vivo study has been done to evaluate its osteogenic properties inside a living organism. For all these limitation, the search for finding a suitable substitute to autograft still continues.

1.9. Experimental Approach and Techniques

In order to design a new osteogenic material for hard tissue engineering, it is necessary to understand the underlying chemistry, material properties, as well as the biological responses to the material. For that reason, some experimental technique gained a lot of attention in tissue engineering field that briefly explained here.

1.9.1. Fourier Transform Infrared Spectroscopy

FTIR is a chemical analysis method based on energy absorption of covalent bonds in a sample. IR radiation excites covalent bonds from a lower vibrational energy to a higher one. This energy can be in a form of vibrational bending, rotating, wagging, stretching, twisting, etc. Each covalent bond can absorb electromagnetic waves at a specific frequency. By monitoring the absorption of IR spectra, covalent bonds in a material can be determined. Note that the exact absorption frequency is not possible to be assigned to a covalent bond because each covalent bond can be affected by many factors; these factors include polarity of neighbor bonds, distortion, three-dimensional

shape, etc. Therefore, a range of frequencies or wavenumbers is attributed to a covalent bond. Alternatively, molecules can be identified by the whole spectrum of absorption as a fingerprint of that molecule. FTIR absorption data always graphs as a dependent variable for “wavenumber”. Wavenumber is a reciprocal of wavelength (wavenumber = 1/wavelength).

1.9.2. Scanning Electron Microscopy

Scanning electron microscopy (SEM) is a microscopy technique that uses a high voltage electron beam instead of an electromagnetic wave to detect objects. SEM scans an object with a focused beam of electron and produces images. When electrons hit the sample they either reflect or scatter. Also, they can knock out an electron from the sample’s atom. By collecting these electrons using a different detector, different information about specimens can be generated including surface topography and surface chemistry.

Secondary electron imaging (SEI) detector collects knocked out electrons from a specimen’s surface. These electrons gain momentum from a non-elastic interaction between the emitted electron and electron form molecule’s K-shell or L-shell. As a result, secondary electrons do not have a high energy and cannot pass through the specimen unless these secondary electrons are very close to the surface. The number of escaped SE depends on the angle of the electron beam with the specimen’s surface. Collection and translation of these SEs can provide a high-resolution image (up to 1nm, depend on the sensor) from the surface of a sample. Due to nature of SEI, acquired

imaged have a high depth of focused field and make it a powerful technique to take images from rough or uneven surfaces in high magnifications.

Backscattered Electrons (BSE) detector collects electrons that scattered from the surface of a sample after being shot by an electron gun. This scattering phenomenon resulted from an elastic collision between emitted electron and atoms of the sample. Heavier atoms are bigger and therefore can scatter more electrons, versus small atoms that scatter less number of electrons. This phenomenon makes it possible to identify atoms and acquire topographical and chemical information from the surface of the sample.

Energy-dispersive X-ray spectroscopy (EDS) is another detector that usually are available in SEM microscopes. When electrons from SEM's electron gun hit the target atom, if the electron energy is high enough it can knock out an electron from inner shells and create an "electron hole." The electron hole will be replaced by an electron from a higher shell which has higher energy. This difference in energy will generate a characteristic X-ray that is unique to that element. By collecting these X-ray beams the element at radiated point can be detected. Mapping elements distribution on the surface is also possible by using scanning electron beam.

SEM rely on electron beams. Therefore to get a reliable and strong electron beam and reduce air interference, the imaging should be done in a vacuum. Furthermore, since high-density electron beam is shooting toward the surface, the surface should be conductive to transfer trapped electrons to the earth. Biological samples are often prone to vacuum and usually are not conductive. Therefore using SEM for these samples could

be challenging. To solve this problem, samples usually become fixated, dehydrated and coated with an electron conductor material to protect their structure and also make them conductive.

There are many electron conductor materials that can be used for coating but the most common ones are carbon and gold. The type of coating material is important when EDS analysis is desired. EDS will capture some signals from the coating material along with signals from the specimen. Therefore, the coating material can interference with the result and generates some artifacts. Carbon coating is usually an effective solution for this problem. Unlike gold it has a low atomic number and does not add unwanted peaks to the X-ray spectrum.

1.9.3. Micro-Computed Tomography

X-ray scanning is a well-known technique that is used in the diagnosis of hard tissue trauma and pathology. A modified version of X-ray scanning is Computed Tomography (CT) scanning. This technique creates a 3D image from a hard tissue by taking multiple sections of x-ray scans and combining them which can provide more information. This technique also is used by scientists as a standard method of collecting μCT results developed for that reason [84]. Micro-computed tomography or "μCT" is similar to clinically used CT scans, but on a smaller scale and significantly higher resolution. High resolution of these machines technically made them a 3D microscopy technique for radio-opaque materials.

1.9.4. Raman Spectroscopy

Raman Spectroscopy is a material characterization method that can characterize functional group and chemical structure of a material. The advantages of this technique over FTIR is that there is no interference between water (OH peak) and other functional groups. This feature makes Raman very attractive for organic tissue characterization since they usually contain a high portion of water and molecules with many –OH groups. Recently, this technique gains a lot of attention among bone biologists as a technique to characterize bone composition [85], evaluate bone maturity, and quantify re-mineralization [86, 87]. Previous studies showed that mature bone in mouse and other rodents has a characteristic Raman spectrum [85]. In this spectrum, there is a band at around 960 cm^{-1} which is related to phosphate. There are also amide I and amide III bands that represent organic components of bone and are located at 1660 cm^{-1} and 1242 cm^{-1} respectively. The intensity ratio of amide I or amide III to primary phosphate band represents the organic to mineral ratio (degree of mineralization) in the bone.

1.9.5. Histology

Histology or "microanatomy" is the study of the biological microstructures from tissues to cells. This is a very powerful technique to study tissue structure, development, and also for diagnostic purposes. Malignant tumors, microbial infection, osteoarthritis, autoimmune disease, and necrotic tissue, all cannot be recognized without the histological examination [12].

To see biological specimen under a microscope, they need to be "fixed." The fixation process stops all cells metabolic activities and stabilizes proteins of the cell

and/or tissue by crosslinking them. This process eventually hardens a tissue and preserve its microstructure. Fixation also, inactivates autolytic enzymes, bacteria, and fungi.

Bright field microscopy is the most common way to study histological structure. For that reason, samples should cut thin enough to let the light pass through it. However, tissue structure still is not hard enough and the sectioning process will disrupt their structure. To make tissue stronger, the water inside will be changed by a harder yet diffusible media like pure paraffin or plastic. Since water is not miscible with embedding medium, it will be replaced by ethanol first through a process called “dehydration.” Ethanol also is not miscible with embedding medium and will be replaced by xylol in “clearing” process. Later on, xylol replaced with paraffin in “infiltration” step and tissue get hardened. Afterward, tissue will be embedded in paraffin or plastic and sectioned in 5 – 15 µm thickness. This process will be done by “Microtome.” At this thickness, most of the structure either is transparent or so dim in colors that make them hard to be identified. Therefore, staining is required to color different region of tissue. Each type of staining dyes binds to a specific region of tissue based on their unique chemical features and color them. This will make the histological section easier to analyze. For staining with water soluble dyes, sections will undergo “rehydration” process which essentially is the reverse of infiltration, clearing, and dehydration process.

1.10. Thesis Objective

The purpose of this thesis is to propose a new system of biomaterial, fabrication method, and implantation procedure to address the current material and methodological limitations in craniofacial reconstruction surgeries.

This thesis had two aims. The first aim was to modify a photo-crosslinkable gelatin silicate nanocomposite for an in-situ 3D (ISP) printing application. This modified composite is called "bio-ink" and consist of crosslinkable methacrylated gelatin (MAG) and laponite (LP). The second aim is investigating the effect of LP and MAG on bio-ink physical properties.

The working hypothesis for the first aim was that incorporating sucrose into photo-crosslinkable gelatin silicate nanocomposite can make it suitable for in-situ 3DP. To assess this hypothesis, many different compositions and printing settings were tested to establish the optimal conditions (the material and the printer setting) for in-situ printing applications. Fourier transform infrared spectroscopy (FTIR), and the optimal ultra violet (UV) intensity for crosslinking were evaluated to analyze successful synthesis and crosslinking in the ISP process. Later, an ISP modified nanocomposite contained MAG, LP, sucrose, and phosphate-buffered saline (PBS) were prepared. Afterwards, the bio-ink was used in cranial reconstruction of a calvarial bone defect of a live rat using ISP technique. To evaluate the effect of in-situ printed bio-ink on bone healing, μCT, scanning electron microscopy (SEM), Raman spectroscopy, and histological analysis was done on treated defect four weeks after surgery. These tests used to characterize healing rate, mineral chemistry and structure of regenerated bone.

The goal was to successfully implement an in-situ printing technique for repairing a critical size defect and induce healing of al rat calvarial bone defect.

The working hypothesis for the second aim was that LP and MAG concentrations control degradation rate, swelling rate and the protein release rate of bio-ink. For testing this hypothesis, different bio-inks that contained 0-20 %wt. MAG, 0-6 %wt. LP, 20% $w/w_{gelatin}$ sucrose, and PBS as a solvent compared in a series of tests to characterize and evaluate bio-ink physical properties. These tests included cell-free degradation, swelling test, and protein release assay. The goal here was to demonstrate the role of LP and MAG in the physical behavior and properties of scaffolds to achieve desired scaffold properties for bone augmentation applications. It is expected that an increase in LP and MAG reduces bio-ink degradation, swelling, and protein release rate.

CHAPTER II

DEVELOPING A SUITABLE INK AND PROCEDURE FOR IN-SITU PRINTING

2.1. Introduction

The goal in this chapter is to develop a method that can treat the bone defect with the least possible delay and without compromising precision in fabrication and implantation. This method possibly can address the limitations in current conventional craniofacial reconstruction methods that were mentioned in section 1.7.

2.1.1. Methodology

As was discussed in section 1.3, micropatterning and microporosity in scaffolds can significantly enhance the bone healing rate of a scaffold by facilitating cell migration and attachment.

3DP is known for its ability to print 3D objects with high precision and producing detailed and high resolution micropatterning within the scaffold. Therefore, it is one of the best candidates to use for making scaffolds for tissue regeneration. However, 3DP still faces some limitations for being used in craniofacial reconstruction. As mentioned in 1.6.2, most 3D printed materials require post-fabrication processing to make them ready for implantation. These post-fabrication processes can be sintering, sterilization, or removal of toxic solvents. Post-fabrication processes increase the cost of surgery, takes time and delay the surgery. In some cases, sterilization after 3D printing is extremely challenging due to scaffold susceptibility to the harsh environment of

conventional sterilization methods. In addition, unplanned changes in the shape of the implantation site during surgery cannot be addressed by using pre-fabricated 3D printed scaffolds.

In this chapter, a novel technique of "in-situ printing" is proposed as an alternative method that can potentially solve above mentioned problems. In-situ printing is a technique of direct 3D scaffold printing into the bone defect of a living organism. In-situ printing can change the bone CSD treatment method from pre-manufactured scaffolds to robotically in-situ printed customized scaffolds. The process includes 3D scanning of the shape of the implantation site, creating a 3D scaffold model using computer software and eventually printing directly into the defect all in one session and during the surgery. Consequently, this feature can potentially eliminate the delay in a surgery or a need for a possible second surgery. In-situ printing is predicted to have high levels of precision, reduce the time of surgery, and be cost efficient. It possibly can eliminate mismatch between the scaffold and the implantation site since all the process will be done after scaffold bed preparation.

2.1.2. Materials

The unique methodology of the in-situ printing (ISP) dictates some specific requirements for the compatible ink. Robocasting, as a selected rapid prototyping method for ISP, requires an ink in a solvent so that it can be solidified after deposition by solvent evaporation or solute crosslinking at biological temperature. In addition, since the printer deposits the material directly on a living tissue, it needs to have no toxic

solvent or solidification process. For this purpose, natural polymers like gelatin could be ideal. Therefore, gelatin was chosen as the matrix of the bio-ink composite.

Ink for the robocasting application should be injectable and have high viscosity. High viscosity gives the extruded filament time to set (solidify) without getting distorted and deformed. Gelation can also affect scaffold printing quality. If the ink turns to gel prior to crosslinking, it cannot handle shear stresses exerted during injection. Consequently, extruded filaments will have unsmooth surfaces and numerous micro-cracks. If the gel strength is too high, the extruded filament can possibly break in several pieces during the printing process and leads to a fragmented filament.

To improve the printability of bio-ink (reducing gelation and increasing the viscosity of methacrylated gelatin or MAG), sucrose was added to the ink. Sucrose was shown to interrupt gelatin gelation by filling the gaps between two polymer chains and weakening polymer chains bonding [88, 89]. This effect makes bio-ink more like a viscous liquid rather than a gel. As mentioned above, gelation can interrupt extrusion (or injection). Therefore, for injecting purposes, a viscose liquid always is preferred to gel. Weaker gelation also means more gelatin can be added to the bio-ink without compromising the composite's homogeneity. Higher concentrations of gelatin increase available sites of crosslinking and consequently increases the number of crosslinks. However, sucrose effectiveness has an optimum concentration and after this optimum, gelation will increase again [90]. This phenomenon can be explained by competition between sucrose and gelatin for water. At low concentrations, sucrose and gelatin would not compete for ionic interaction with water molecules. On the other hand, at high

concentrations less water is available for both and sucrose and gelatin would compete for limited available binding sites of water molecules. This competition for water results in a tenderness and high gelation behavior of the solution.

As was mentioned in section 1.8.3, pure gelatin does not possess osteogenic properties. To induce osteogenic property, gelatin is usually composited with silicon-based ceramics. Among these ceramics, LP showed promising results in healing bone defects. Therefore, MAG-LP composite was chosen as the base of the ink used for the ISP method in this study.

Since printing will be performed directly on a live animal's tissue, using organic and toxic solvents can compromise the healing process. Therefore, a system of crosslinking with the lowest possible cytotoxicity should be used for ISP. One of the crosslinking system with the least cytotoxicity is based on carbon-carbon double bonds opening using free radicals generated by ultra violet (UV) light. C=C does not exist in gelatin, therefore through an addition reaction, methacrylate, which has C=C, was grafted to gelatin and convert it to MAG.

To initiate the crosslinking reaction, a photoinitiator is used. Photoinitiators are a type of crosslinking agent with a linear molecule structure and two special functional group at their two ends. These functional groups are unstable and in the presence of UV light lose electrons and become free radicals. Free radicals at the two ends of the photoinitiators can readily react with two C=C groups from different MAG and crosslink them together [75]. There are many different photoinitiators in the market for different purposes. Since the process of crosslinking in ISP occurs in the biological environment,

the photoinitiator used for this application should have low cytotoxicity. Studies showed 2-hydroxy-1-(4-(hydroxyethoxy)phenyl)-2-methyl-1-propanone, also known as IRGACURE 2959 (I2959), has the lowest cytotoxicity among other available photo-crosslinking agents [91]. This photoinitiator can generate radicals and initiate the crosslinking reaction in the presence of 365 nm UV light illumination.

MAG was synthesized and its successful methacrylation reaction was confirmed by Fourier Transform Infrared Spectroscopy (FTIR). Different printing settings were tested to achieve the optimal setting for ISP application. Also, different concentrations of sucrose and LP were tested in order to achieve a uniform and stable scaffold. The minimum UV intensity required for complete crosslinking of the bio-ink were evaluated. Later on, the optimized bio-ink was used for the in-vivo study. These in-vivo studies involved in-situ printing into calvarial bone defects of live rats to evaluate the effect of in-situ printed modified material (bio-ink) on bone healing. Micro-CT, Scanning Electron Microscopy (SEM), Raman spectroscopy, and histological analysis was done to characterize healed region's mineral chemistry and microstructure.

2.2. Materials and Methods

2.2.1. Sterilization Using Ethylene Oxide

Due to the presence of sucrose and gelatin, bio-ink is highly vulnerable to bacterial and fungal growth. Therefore, before preparing bio-Ink, all ingredients were sterilized by ethylene oxide (EtO) for 24 hours and desiccated for an additional 24 hours to remove virtually all residual ethylene oxide. Ethylene oxide is a highly toxic; treated

materials should stay in a low-pressure environment after the sterilization process to remove all diffused gas. Ethylene oxide was chosen for sterilization because of its less harsh temperature and pressure requirement relative to other sterilization methods which keep MAG fairly undamaged [92]. All bio-ink preparation was performed in biosafety cabinet to reduce the chance of any contamination.

2.2.2. Methacrylated Gelatin Synthesis

0.1 gr/ml powdered cell culture tested gelatin from porcine skin with a Bloom Index of ~300 (G1890 Sigma) was mixed with Dulbecco's phosphate buffered saline or DPBS (21-031-CV CORNING cellgro) at 60$^{\circ c}$ and stirred for 20 minutes to dissolve the gelatin completely. Later on, the temperature was reduced to 50$^{\circ c}$ and 0.8ml methacrylate anhydride or MA (276685 ALDRICH) per each gram of gelatin was added to the solution under a continuous stirring condition at a rate of 0.5 mL/min. After adding MA, the solution was kstirred for 3 hours. Figure 3 illustrates the methacrylation reaction.

Later on, the solution was transferred to 12-14 kDa dialysis tubes (Spectra/Por® 4, Dialysis Membranes, MWCO 12000 to 14000, Spectrum® Laboratories INC) and dialyzed against ultrapure DI water (MILLIPORE MILLI-Q PLUS ZD5211584) at 18.2 Ω. The dialysis system was stirred continuously for a week at 40$^{\circ c}$ to filter unreacted reagents. The water was changed every day to maintain osmotic pressure in the system. The purified solution was transferred to a freeze-dryer (LABCONCO FreeZone 2.5) and lyophilized for 1 week to isolate MAG and then stored at ~ -80$^{\circ c}$ to preserve the lyophilized MAG.

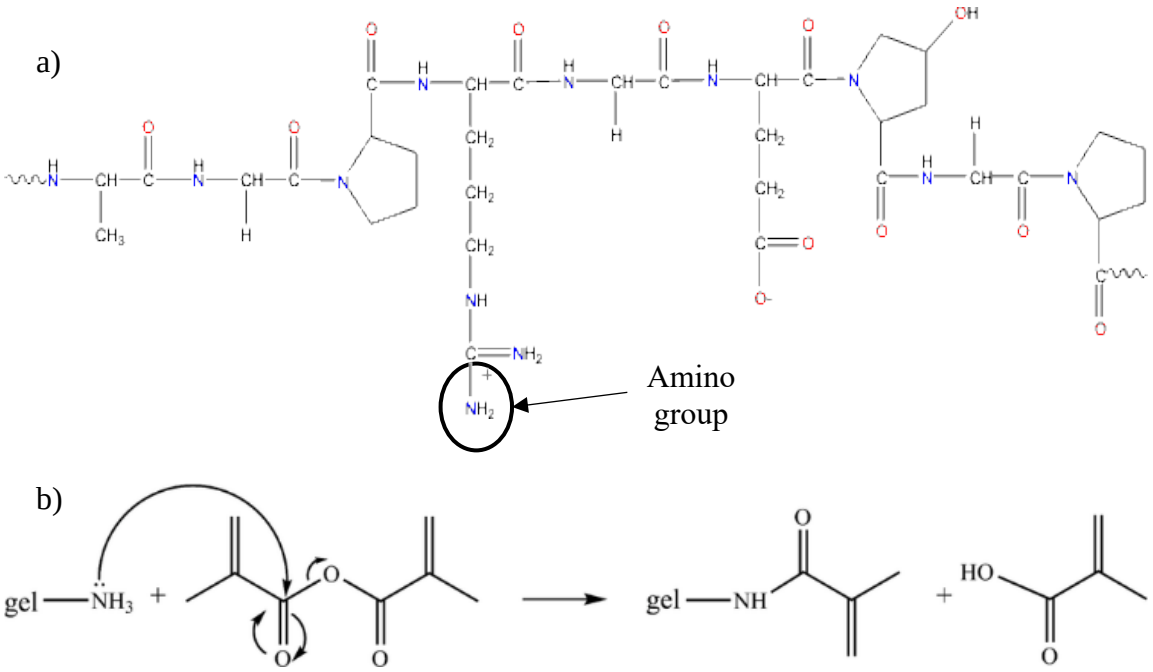

Figure 3. (a) The structure of a gelatin monomer. Note that a gelatin monomer has only one amino group, but a polymer chain of gelatin has many amino groups on the backbone. (b) The chemical reaction of gelatin and MA. Note that in this reaction, an amino group converts to an amide group.

After synthesis of each batch, samples were analyzed by FTIR (Thermo SCIENTIFIC NICOLET iS10 SMART iTR) to confirm successful methacrylation.

2.2.3. Adjusting Material and Printing Setting

As mentioned previously, ISP needs both a modified ink and an adjusted printing setting to become compatible for the unique warm and wet conditions of the ISP environment (living tissue). Since ISP is a new technique, there is no modified material or printing protocol designed for it. Parameters that can affect printing that needed to be adjusted are printing speed, extrusion speed, materials gelation, trapped air inside the ink, rod-rod distance in the scaffold, Z-distance between each printed 2D layer, and Z-distance from the substrate at the printing starting point. Some of these parameters

depend on each other and so changing one, will require some adjustment of the other. For example, extrusion speed and printing speed have a direct relation; an increase in extrusion speed requires an increase in printing speed to prevent filament distortion. To adjust the MAG-LP composite for ISP, two factors need to be considered: temperature and viscosity. The temperature will reduce gelation and viscosity of the ink [93].

To adjust the printing setting, the algorithm in Figure 4 is followed where one parameter was changed while the rest were fixed and the effect on printing was evaluated. Based on these data, a new setting was suggested and tried. If it did not work, the problem was identified and based on that, a new modified setting was suggested.

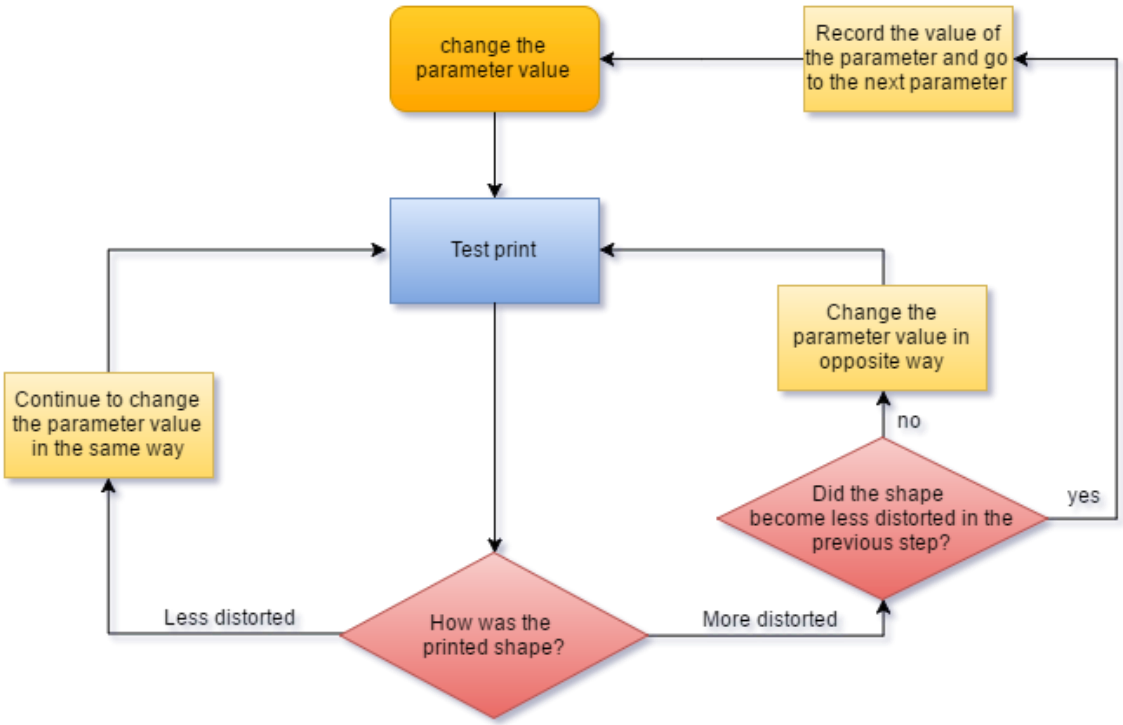

Figure 4. The schematic of the algorithm used for modifying printer's values.

The filament diameter should be thin enough to make it possible to produce more pores in a unit of volume. However, too thin a filament will compromise the scaffold integrity and distort it easily. A 0.2 mm dispenser inner diameter was chosen for this purpose. Ideally, the plunger movement will define the extrusion speed at the tip of the dispenser by assuming that ink has hydraulic behavior (it cannot be compressed). Volume reduction in the tube resulted from plunger movement should be equal to the volume of extruded filament. This concept can be formulized into the equation:

$$V_p \times D_t = V_f \times D_f \qquad \text{(Equation 1)}$$

Where V_p is the plunger speed, D_t is the dispenser tube diameter, V_f is the filament extrusion speed, and D_f is the filament diameter.

The printing speed should be adjusted according to "filament extrusion speed." Slower printing speed than filament extrusion speed will result in accumulation and distortion of extruded filament and faster printing speed will result in overstretching and tearing of filament.

The results are reported as successful or unsuccessful printing and a reason for the unsuccessfulness was determined.

2.2.4. Bio-ink Preparation

0.5% w/$w_{(MAG)}$ I2959 was added to pre-heated DPBS (at 50$^{\circ c}$) and mixed. Next, Lp (Laponite XLG, BYK Additives Inc. Texas, USA) and sucrose (S0389 SIGMA) were gradually added to the solution under continuous stirring conditions. Sucrose was added in a ratio of 20% w/$w_{(MAG)}$. The solution was stirred at 50$^{\circ c}$ for 15 minutes. Afterward, a pre-weighted MAG was added to the solution and transferred to a Planetary Centrifugal

Mixer (THINKY ARE-310) and mixed for 15 minutes at 2000 rpm and defoamed for one minute at 2200 rpm. Figure 2 shows a schematic process of bio-ink preparation in micro scale. After mixing, the nanocomposite was transferred to a 3cc UV protected dispenser tube (Nordson EFD Optimum® Light Block AmberBarrels), sealed and centrifuged for one minute at 4.4 krpm to remove all the air trapped inside the ink. This is a very crucial step; if the syringe is not properly de-bubbled, the continuous material injection in the robocaster will be interrupted, the filament will rupture and the whole scaffold will distort.

2.2.5. Minimum UV Intensity for Bio-ink Crosslinking

The crosslinking process is initiated by UV light and the degree of crosslinking has a direct relation with UV light intensity [94]. To determine the optimum UV light intensity, scaffolds with dimensions of 6 x 8 x 6 mm were printed (The average weight of scaffolds at this size was measured 0.10 gr < x < 0.15 gr) with a printing speed of 9 mm/min. While printing, injected material was exposed to a UV spotlight right at the tip of the printer's nozzle (THORLAB CS2010). Five groups were designated and each group was treated with a different light intensity (5, 10, 20, 30, 40 mW/cm^2). After printing, samples were transferred to wells filled with 4ml PBS and incubated at $37^{\circ c}$. During incubation, scaffolds were monitored for any sign of dissolution and degradation. The degradation rate of Bio-ink is directly related to the degree of cross-linkage [94]. At $37^{\circ c}$, up to 5% wt. gelatin can readily be dissolved in water without creating a gel [95]. Therefore, to eliminate the effect of gelation on the test, the total weight of scaffold in

the media was keep below 5% of the PBS. As a result, each scaffold was incubated in 4 ml PBS.

To run the test, a bio-ink is selected that can be dissolved fairly fast in an uncrosslinked state. Therefore, it can make scaffolds gross changes easier to track and also contain all the ingredients of bio-ink. Since the dissolution of bio-inks with a higher concentration of MAG or LP usually increases the viscosity of the solution and slow down further dissolution, a composition with a lower concentration of MAG and LP was more proper for this test. As a result, a 2-10 bio-ink (2% LP, 10% MAG, 2% Suc, 0.05% I2959) was selected for this test.

2.2.6. Partial Removal of Rat's Calvarial Bone

Defects with dimensions of 4 ± 1 mm by 6 ± 1 mm was created on the right side of the sagittal suture on a rat's calvaria according to the IUCUC approved protocol #2014-0153. One year old male Sprague Dawley rats (about 430 gr each) were purchased from Envigo. A total of 18 rats (three for each test group) were used in this study and one scaffold per animal was implanted to have triplicate samples for evaluation. The partial removal of calvarial bone procedure is explained below.

The rat was anesthetized with 5% isoflurane (Henry Schein) with a flow rate of 4-5 L/min until breathing speed dropped to about half. Then, the rat's head was shaved from caudal end of the skull to the bridge between two eyes. Later on, its head was fixed on a stereotaxic device and an oximeter/heart rate monitor clip attached to its leg. Afterward, the isoflurane concentration was reduced to 1-2% and delivered to the rat

through a nasal mask. The rat's heart rate was constantly monitor and kept between 225-300 bpm.

A 1.5cm sagittal incision from forehead to the caudal end of the skull was created by scalpel blade #15 and the periosteum layer was scratched away to expose the bone. The bone was irrigated by sterile saline solution and then dried by sterile gauze and air blowing. The defect's boundaries were drawn on the calvaria using a sharpie and a template. Later on, the bone was gradually cut using high-speed dental handpiece with #1 round carbide dental burr. The cutting was continued until a pinkness become visible on the drilling lines. A forceps was used as a leverage to lift the bone. Figure 5 shows the process of cutting the bone. Later on, the exposed dura was cleaned and dried. This bone cutting process is very delicate and the burr can damage the dura if it passes all the way through the bone. Damage to the dura may cause some serious damage to the rat's brain and/or bone healing process.

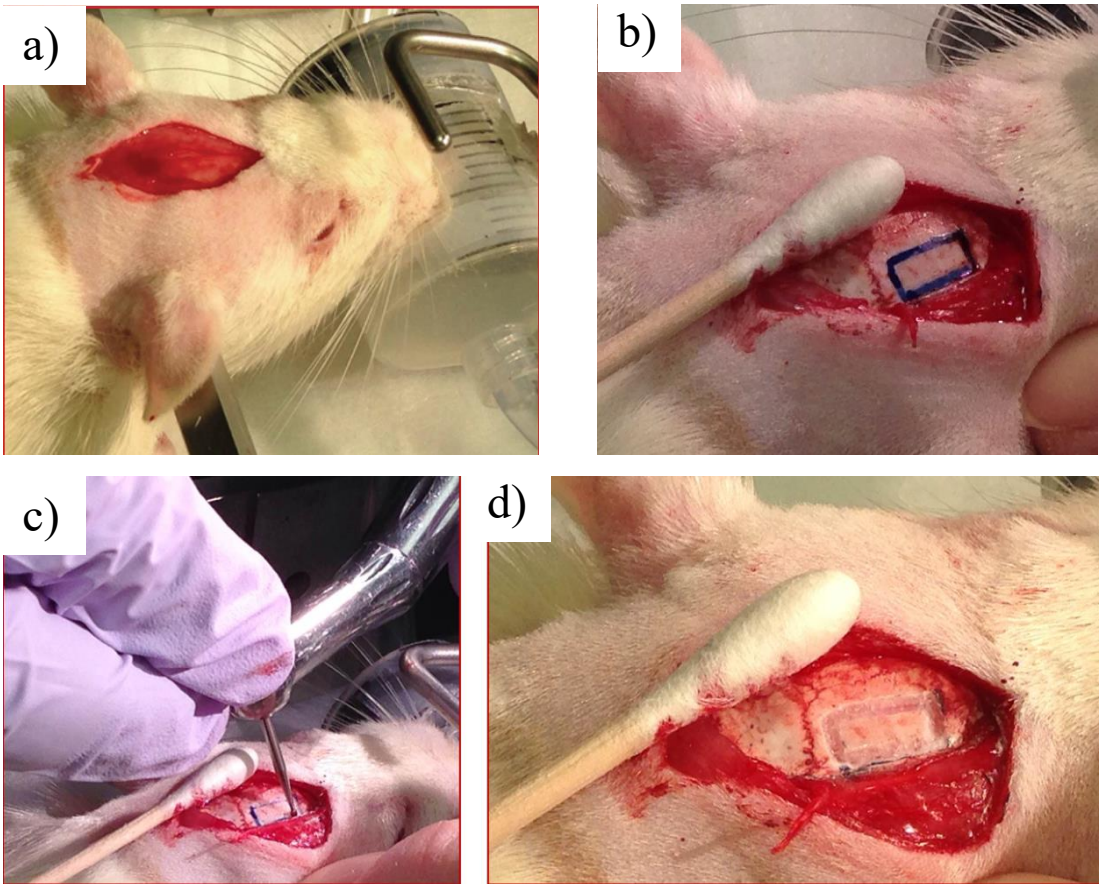

Figure 5. Creation of defect in a rat's calvarium. (a) Making an incision in skin and periosteum (b) Drawing defect's boundaries using a template (c) cutting the bone using dental burr (d) bone is thinned enough that it can be lifted off. Reprinted with permission from [96].

2.2.7. Proposed In-Situ Printing

To evaluate the effect of bio-ink and in-situ printing, six different treatments for healing rats' calvarial bone defect were implemented: empty defect or no treatment (served as control), implantation of pre-fabricated bio-ink of 2-10 (current conventional implantation method served as a treatment control), implantation of pre-fabricated FDA approved 30%PCL-70%TCP composite hybrid, in-situ printing of the 2-10 bio-ink and in-situ printing of a 4-10 bio-ink (4% LP, 10% MAG, 2% Suc, 0.05% I2959). All treatments were done in triplicate. 4 weeks after surgeries, calvarial bones were

harvested and cutted coronally into two halves. One half of a sample was used for Histological analysis and the other half was used for SEM. Raman, and micro-CT analysis.

To perform ISP first, the bio-ink filled dispenser tube was installed on the 3D printer and a gauge 30 (0.2mm) dispenser tip was attached to it. Afterward, the rat was transferred to the printing area of the robocasting machine according to Figure 6.

The printer's probe was brought lower along Z-axis of the printer (height) until the dispenser tip touched the dura on the lateral side of the defect and the coordination was recorded. This step was repeated on the medial, rostral and caudal sides of the defect. If these measurements showed that dura was not horizontal and was tilted, the stereotaxic device was adjusted accordingly to make the dura's plane horizontal. By this action, the Z-axis coordination of dura also was achieved. The shape, position, and size of the defect are recorded by moving the dispenser tip along Y- and X-axis of the printer and touching the side walls of the defect and recording the coordinates. The thickness of the bone was measured by subtracting the coordination of the top surface of the bone and the surface of the dura.

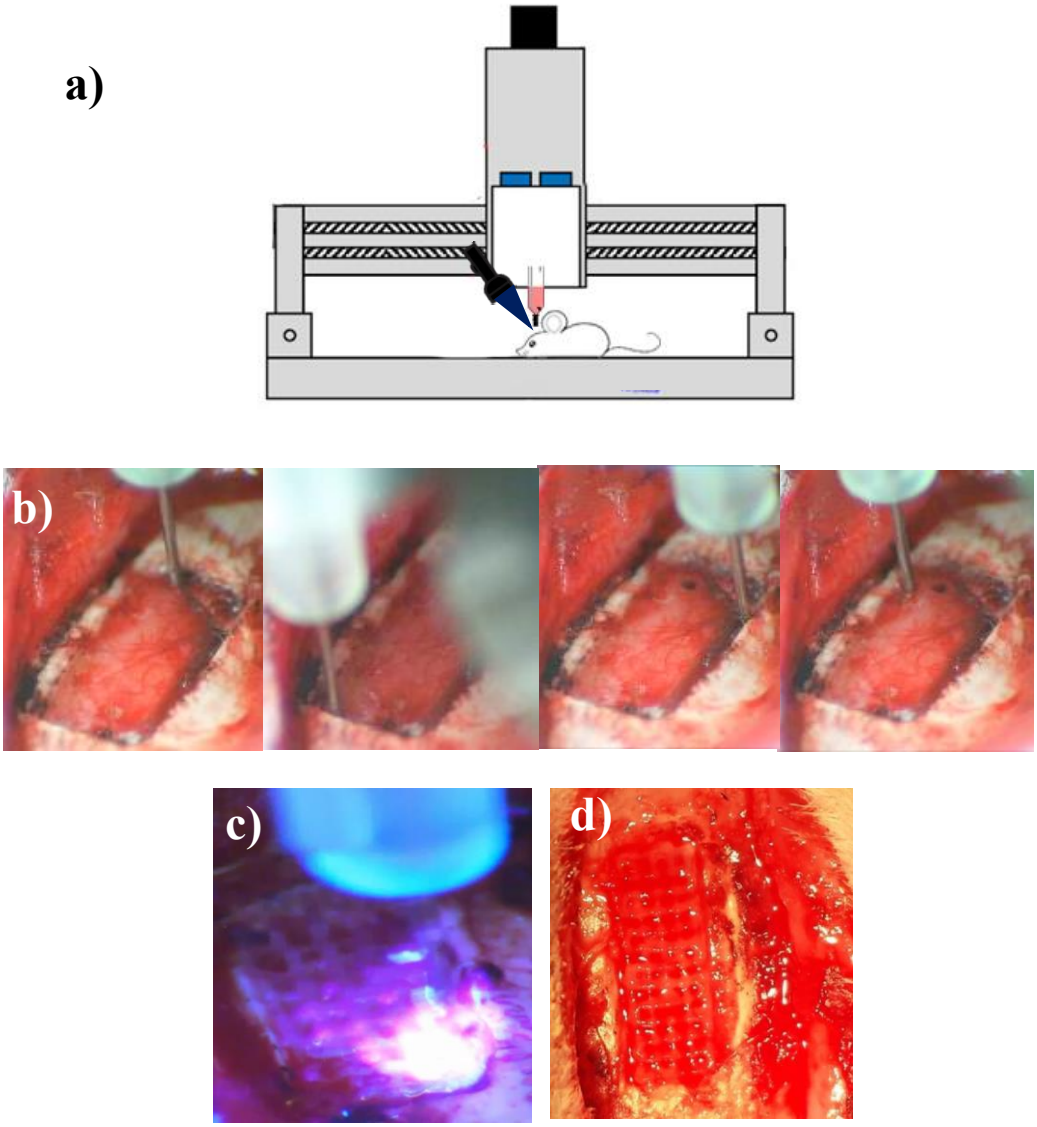

Figure 6. (a) The schematic shape of in-situ printing, a UV spotlight is continuously crosslinking scaffolds as they extruded out. (b) The process of recording the coordination and the shape of a defect (calibration) by hitting bone's wall and recording their relative position. (c) in-situ printing in progress (the bright blue light is the UV spotlight illumination at the tip of the dispenser. This spotlight had a diameter of 2mm) (d) the final outcome of in-situ printing before suturing the incision.

Based on recorded coordinates, a suitable shape for a scaffold was designed. The scaffold was designed to be 0.2 - 0.4 mm smaller in length and width to give the printed scaffold a margin of 0.1 to 0.2 mm from each side of the defect. The printing setting was

set for a printing speed of 9 mm/s, pore size (rod to rod distance) of 0.65 mm, and layer deposition with a thickness of 0.15 mm. The number of required layers was calculated by dividing the bone thickness by depositing layer thickness (thickness of bone (mm)/0.15). A margin of 0.1 to 0.2 mm was considered for scaffold swelling after absorbing blood and serum in the periphery. The printing speed was adjusted based on the viscosity of the bio-ink and the speed that the material extruded out from the dispenser tip. This number was determined experimentally according to section 2.2.3. As discussed before, the optimum pore size of the scaffold for cell migration was 0.5 mm. The printing filament had a thickness of 0.2 - 0.15 mm. Therefore, a rod-rod distance of 0.65 mm would give a pore size close to 0.5 mm. The starting position for printing was determined in a way that the dispenser tip was 0.15 mm above the dura. This distance is designated for the first depositing layer.

To verify the printing process and the pressure inside the dispenser, a test print on a sterile, flat surface was performed. The 365nm UV spotlight with a diameter of 2 mm was adjusted to directly illuminate the tip of the dispenser with an intensity of ~ 31 mW/cm^2 to crosslink material as it extruded out. After checking all parameters and coordination, in-situ printing was started. When in-situ printing was finished, the printed scaffold was irrigated by PBS to wash all unreacted reagents. Later, the flapped skin was sutured with 4-0 braided silk suture and the incision area cleaned by saline and sterile gauze. At that time, the isoflurane concentration reduced to zero. When the animal's heartbeat started to increase, a 0.1ml of painkiller (nalbuphine) was injected intramuscularly.

If for any reason printing was not successful, it was immediately stopped, the defect cleaned by a sterile gauze, dried by air, and the printing was repeated.

2.2.8. Scanning Electron Microscopy

In this study, BSE was used to analyze the chemical composition and surface microstructure of scaffolds and dissected bone and EDS was used to determine elements distributions on the surface of dissected bone and scaffold. The SEM machine used for these tests was JEOL - JSM-6010LA (USA, Peabody, MA) and carbon used for coating samples to minimize the coating layer interference with EDS analysis. EDS analysis were performed at 10 kV, spotsize of 80, and working distance of 8 mm to keep dwell time above 7000. BSE image were taken at 20 kV and high vacuum conditions.

2.2.9. Micro-Computed Tomography

In this study μCT scanning was done on harvested calvaria to analyze the amount of regenerated bone and also the pattern of healing in the region. All μCT works were done using the Scanco Medical 3.5 μCT. The unit performed serial x-ray tomographic imaging at the density of 20 cross sectional slices per 100 μm, an energy level of 55 kV, and intensity of 145 μA. The lower and upper threshold values used for this analysis were 280 and 1000 respectively. The remineralization percentage was calculated by divided the area of unmineralized tissue by the area of initial defect. For calculating the area NIH's ImageJ 1.15b was used.

2.2.10. Raman Spectroscopy

Raman spectroscopy (DXR, Thermo Scientific, 10x objective) was done on coronal section of calvaria samples to evaluate the quality and chemistry of regenerated

bone and also to provide a better understanding of the healing pattern and fate of the scaffold in the defect. Four different spots around remineralization front (RMF) including surrounding bone (SB), remineralized tissue, RMF, and fibrous tissue were analyzed. These data were then compared with the data from crosslinked bio-ink. To minimize tissue fluorescence, 780 nm laser and slit spatial filter was used. The diameter of the analyzed spot was 1µm. The samples were photobleached for 4 minutes prior to spectra collection and a 10 s exposure time was used. Thirty two spectra per location were recorded between 400 and 2000 cm^{-1}.

2.2.11. Histology

For the purpose of this study, coronal section of specimens stained with Hematoxylin and Eosin (H&E) and Stevenel's Blue with Van Gieson Picro-Fuchsin counterstain (or in short, Stevenel's Blue). H&E is a powerful method to study cells behavior and organic components of bone and connective tissue. On the other hand, Stevenel's Blue is a useful technique to study hard tissue's histology. Hematoxylin has blue/purple color and binds to basophilic components like nucleic acids. Eosin has red color and binds to acidophilic components like proteins. Stevenel's Blue stains connective/fibrous tissue blue-green and osteoid light green. Van Gieson counterstain stains bone sharp red.

Prior to sample preparation for histology samples were fixed in absolute ethanol. Specimens were desiccated for the purpose of another study; this situation can deform histological structure and produce artifacts in images. Therefore, specimens rehydrated by immersing them in PBS at $37^{\circ c}$ for two days.

For H&M staining, samples were decalcified in 0.5 M EDTA (ethylenediamine tetraacetic acid, tetrasodium salt). Tissues then were x-rayed every two weeks to monitor the decalcification process. When all the mineral tissues have been removed, the specimens were dehydrated, cleared, and infiltrated. Dehydration was done by immersing specimens in 50%, 70%, 80%, 80%, 95% ethanol (EtOH) respectively and each for 30 minutes; then leave them in a 95% EtOH over a night and then specimens to absolute EtOH for an hour. Specimens cleared by immersing them in xylene for one hour and later they infiltrated by immersing in melted paraffin for two hours under the vacuum. The tissues were next embedded in paraffin blocks at $60^{\circ c}$ and sectioned at 6 microns using microtome (Leitz 1512). The sections were then mounted on coated glass slides and dried at $42^{\circ C}$ for 2 hours and then overnight at $54^{\circ C}$. Next, to stain samples with Hematoxylin and Eosin stain slides were immersed in xylene, absolute EtOH, 95% EtOH, deionized water, hematoxylin, water, ammonia, water, eosin, 95% EtOH, absolute EtOH, and xylene for 20, 2, 4, 3, 1, 3, 2, 3, 1, 5, 6, 6 minutes respectively. Next, a few drops of Permount mounting medium (Fisher Chemical™) were applied on the slide and covered by a glass coverslip.

For Stevenel's blue staining, after rehydration, samples were immersed in 50%, 70%, 95%, and 100%, EtOH for 3, 1, and 7 days respectively to dehydrate them. Samples next immersed in acetone for a day and methyl methacrylate monomer for 4 days. To embed samples first methyl methacrylate semimer was made by mixing 200 ml of MMA monomer and 2 g of benzoyl peroxide at $40^{\circ C}$ for around 2 hours until semimer developed and become viscose. Samples then embedded in semimer until polymerization

become completed. Samples next sectioned by low speed Saw using Isomet Saw (series 15LC, Buehler - Houston, TX) and at a thickness of approximately 150 microns and the grinded and polished to around 75 micron. For staining, samples stained with preheated Stevenel's Blue stains at for 20 minutes and rinsed in water and then stained with Van Gieson picro-fuchsin staining for 5 minutes at room temperature.

2.3. Results

2.3.1. Fourier Transform Infrared Spectroscopy

Figure 7 shows the FTIR results from the synthesized MAG, gelatin and crosslinked bio-Ink. This figure showed amide I peak at 1630 cm^{-1} and amide II at 1520 cm^{-1} in the gelatin spectrum. These amide peaks can be found in a collagen (gelatin) structure [97]. In the synthesized material spectrum, amide II peak shifts toward 1537 cm^{-1}. In the synthesized MAG spectrum, a shoulder at ~1650 cm^{-1} is visible which was not detected in the crosslinked ink spectrum. The spikes at 990 cm^{-1} and 1068 cm^{-1} are known as signals for Si-O ad Si-O-Si respectively [98].

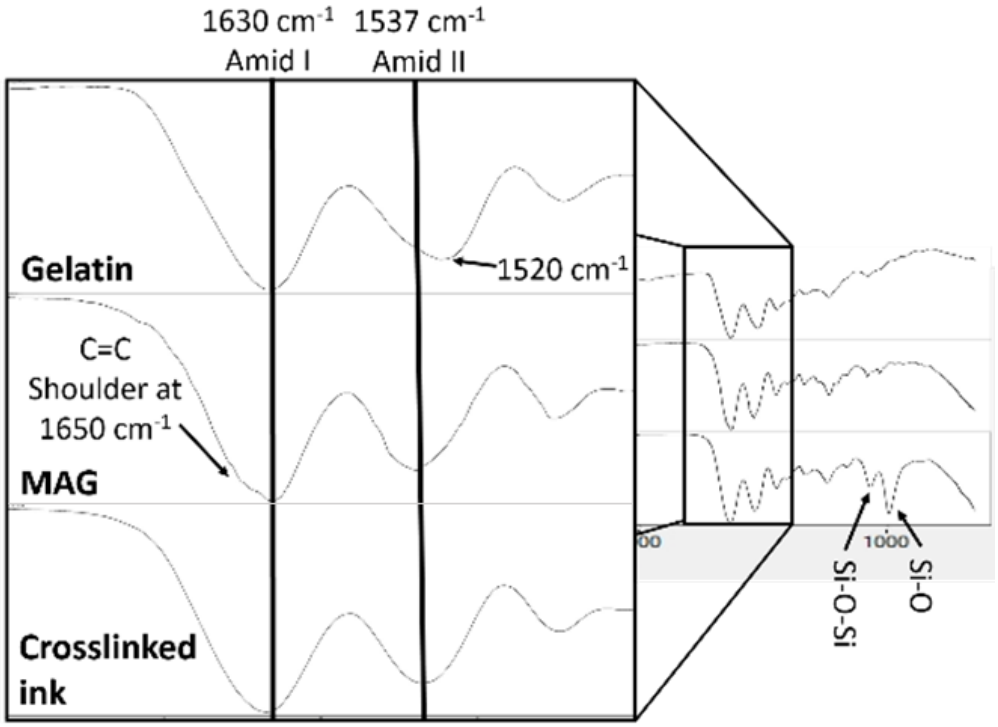

Figure 7. FTIR Spectroscopy from gelatin, MAG and crosslinked bio-ink. Without magnification, the overlap between amide I peak and C=C makes it hard to distinct these two peaks.

2.3.2. Adjusting Material and Printing Setting

The optimum setting and material composition for ISP was achieved by evaluating different setting through many trials. The summary of all attempts are listed in Table 1, Table 2, Table 3, Table 4, and Table 5. For each setting, a set of 10 to 15 attempts was done. For each attempt, scaffold's shape was different (cylinder, cubic, and rectangular prism with different dimensions). If all attempts failed, the result recorded as unsuccessful printing. If more than one attempts but not all succeeded, the result recorded as successful printing but with low consistency. If all attempts were successful, the result recorded as successful printing.

Table 1. Attempts to adjust the centrifuge speed and duration to remove the trapped air in the ink

Centrifuging to remove trapped bubble			
	Successful printing	If no, reason	Suggestion
1 Krpm for 1 min	No	Trapped bubble caused segmented extrusion	Using higher centripetal forces or longer centrifuge time
1 Krpm for 2 min	No	Trapped bubble caused segmented extrusion	Using higher centripetal forces or longer centrifuge time
1 Krpm for 5 min	No	Trapped bubble caused segmented extrusion	Using higher centripetal forces or longer centrifuge time
2 Krpm for 5 min	No	Trapped bubble caused segmented extrusion	Using higher centripetal forces or longer centrifuge time
3 Krpm for 5 min	No	Trapped bubble caused segmented extrusion	Using higher centripetal forces or longer centrifuge time
4.4 Krpm for 5 min	No	Trapped bubble caused segmented extrusion	Reduce centrifuge time
4.4 Krpm for 2 min	Yes	N/A	N/A
4.4 Krpm for 1 min	Yes	N/A	N/A

De-bubbling, plunger speed, and printing speed trials were done on all four different compositions to evaluate the optimum setting for each (if it was possible to find). All four compositions behaved similarly in these attempts.

Table 2. Attempts to adjust bio-ink composition for the most reliable printing

Composition			
	Successful printing	**If no, reason**	**Suggestion**
No Suc, 2%LP (0.3mm pore size)	No	Filaments fused in each other	Increase viscosity by increasing LP conc.
No Suc, 2%LP (0.5mm pore size)	Yes, but not consistent	In some areas, filaments fused in each other	Increase viscosity by increasing LP conc.
20% Suc, 2%LP (0.3mm pore size)	No	In some areas, filaments fused in each other	Increase viscosity by increasing LP conc.
20% Suc, 2%LP (0.5mm pore size)	Yes, but not consistent	In some areas, filaments fused in each other	Increase viscosity by increasing LP conc.
No suc, 4%LP (0.3mm pore size)	Yes, but not consistent	occasionally the filament was segmented	Reduce gel strength by adding sucrose
No suc, 4%LP (0.5mm pore size)	Yes, but not consistent	occasionally the filament was segmented	Reduce gel strength by adding sucrose
20% Suc, 4% LP (0.3mm pore size)	Yes	N/A	N/A
20% Suc, 4% LP (0.5mm pore size)	Yes	N/A	N/A

Table 3. Attempts to evaluate the optimum distance between substrate and dispenser tip

Z-distance from the substrate at printing starting point			
Tip and substrate distance	**Successful printing**	**If no, reason**	**Suggestion**
Touching the substrate	No	The material was not extruded. A pressure built up and a burst extrusion happened in the second layer.	Increase the distance
0.1 mm	Yes, but the first layer was distorted	Filaments of the first layer were flattened and merged. Other layers were printed with no problem	Increase the distance
0.15 mm	Yes	N/A	N/A
0.2 mm	No	The filament did not stay on to the substrate and moved as printer moved	Decrease the distance
Z-distance between each printed 2D layer			
Average distance between layer	Successful printing	If no, reason	Suggestion
0.2	No	Filaments cannot stick to bottom layers	Increase the distance between layers
0.15	Yes	N/A	N/A
0.1	Yes, but resolution was reduced	The filament slightly flattened that caused a reduction in pore size	Decrease the distance between layers

Table 4. Attempts to modify plunger speed

Plunger speed			
plunger speed	**successful printing**	**If no, reason**	**Suggestion**
0.5 mm/min	No	After a few layer, a built up pressure ejected the dispenser tip	Reduce the plunger speed
0.4 mm/min	No	After a few layer, the material leaked out from the sides of the dispenser tip	Reduce the plunger speed
0.3 mm/min	Yes	N/A	N/A
0.2 mm/min	No	The extrusion speed was too slow	Increase the plunger speed
0.1 mm/min	No	Ink did not extrude out in the entire printing process	Increase the plunger speed

It is noted that higher concentrations of MAG and LP that were used in the next chapter also went through printer speed trial, and the 6-20 bio-ink (6% LP, 20% MAG, 4% Suc, 0.1% I2959) was the only composition which had the optimum printing speed

of 6 mm/min. the rest of the bio-inks had successful printings using the chosen setting in this chapter.

Table 5. Attempts to adjust printing speed for the most replicable results

Printer speed at plunger speed of 0.3 mm/min			
Printing speed	Successful printing	If no, reason	Suggestion
14.75 mm/min	No	The filament stretched and broke	Reduce the printing speed
12 mm/min	No	The filament stretched and broke	Reduce the printing speed
10 mm/min	Yes, but not consistent	There were some occasional segmentations	Reduce the printing speed
9 mm/min	Yes	N/A	N/A
8 mm/min	No	Couldn't print straight filaments	Increase the printing speed

By summarizing the results, the most consistent and successful result was for a bio-ink with 20% $w/w_{gelatin}$ Sucrose and 4% wt. LP, centrifuging with 4.4 Krmp for 1 minute, dispenser tip to substrate distance of 0.15 mm, plunger speed of 0.3 mm, and printing speed of 9 mm/min.

2.3.3. Minimum UV Intensity for Bio-ink Crosslinking

Crosslinking tests on bio-ink revealed that as UV intensity increases, the scaffold can hold its integrity for a longer time. Figure 8 shows that scaffolds crosslinked with light intensity below 21 mW/cm^2 completely dissolved in PBS in less than five days. The scaffold crosslinked by 21 mW/cm^2 also shows some signs of deformity and hyper-swelling. Scaffolds crosslinked by 31.5 and 42 mW/cm^2 stayed intact in the environment for 11 days. Note that there is a color difference between scaffolds crosslinked with UV intensity above 21 mW/cm^2 and those crosslinked with lower intensity.

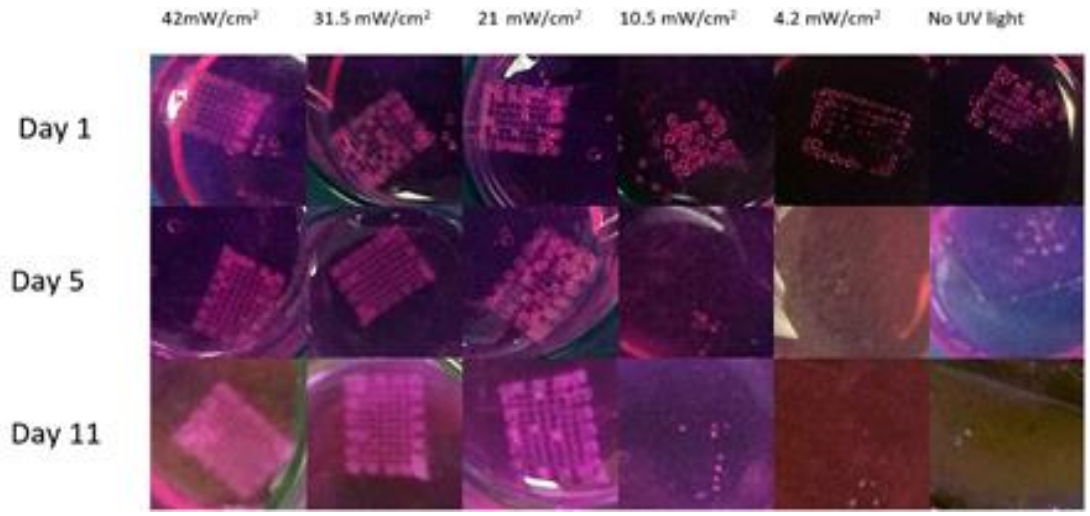

Figure 8. Effect of real-time UV illumination intensity on Bio-ink solubility.

2.3.4. Scanning Electron Microscopy

Backscatter SEM images from a coronal section of the defect are shown in Figure 9. Dark areas belong to elements with a low atomic number (like carbohydrates). Bright areas belong to elements with a relatively higher atomic number like inorganic atoms (Ca, P). There are some bright dots in the dark region (arrow in Figure 9) and also some islands composed of heavier atoms (Figure 9.b). Also, in Figure 9.c heavy elements and light elements diffuse in each other and there is not a clear boundary.

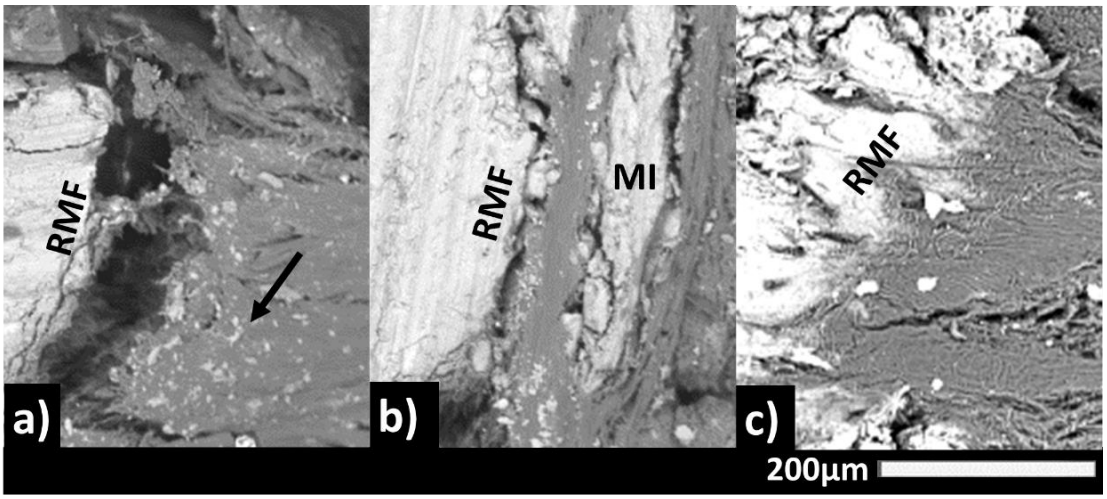

Figure 9. Backscattered Scanning Electron Microscopy (BS-SEM) from a coronal section of the defect shows the area around remineralization front (RMF).

EDS mapping analysis from a coronal section of harvested calvaria showed that the defect is not fully healed (Figure 10. a). It also showed that hard regenerated tissue contains calcium and phosphorous. Note that the scaffold did not contain either Ca or P (Figure 10. b). It also showed that there is no Si trace in either regenerated or fibrous region of defect (Figure 10. a). However, the scaffold itself contain a detectable amount of Si (Figure 10. b).

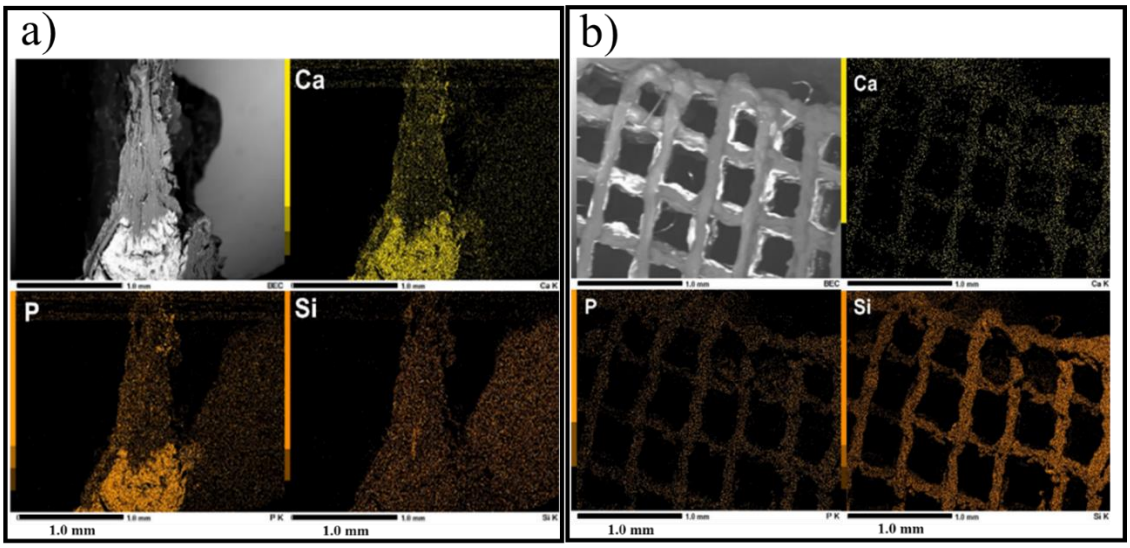

Figure 10. (a) EDS analysis from a coronal section of a harvested calvarium. This mapping was done 4 weeks after in-situ printing of the 4-10 bio-ink and showed Ca and P in regenerated hard tissue and no detectable amount of Si in both hard and fibrous region. (b) EDS analysis of crosslinked bio-ink scaffold showed the presence of Si all over the scaffold and no Ca and P.

2.3.5. Micro-Computed Tomography

Micro-CT imaging from calvarial bones (Figure 11) showed that empty-hole control treatment exhibits 11% remineralization in 4 weeks. This was the lowest healing rate among all treatments ($P < 0.05$) but does not have any significant difference with pre-fabricated 30% PCL - 70% TCP composite. The PCL-TCP composite produces some minor healing, but showed signs of bone resorption in defect site (arrows Figure 11). On the other hand, the pre-fabricated 2-10 bio-ink showed an increase in remineralization at 4 weeks versus empty-hole treatment ($P < 0.05$). Furthermore, in-situ printed scaffolds with the same bio-ink composition of 2-10 showed near 44% improvement in bone healing that was higher than PCL-TCP treatment. In another treatment, scaffolds with the in-situ printing of the same bio-ink but with doubled concentration of LP (4-10) has been used and it was able to heal more than the pre-

fabricated 2-10, PCL-TCP, and empty hole. The same treatment was used for the last group but calvaria were harvested 6 weeks after the surgery. It was shown that there is no difference in healing between 4 and 6 weeks.

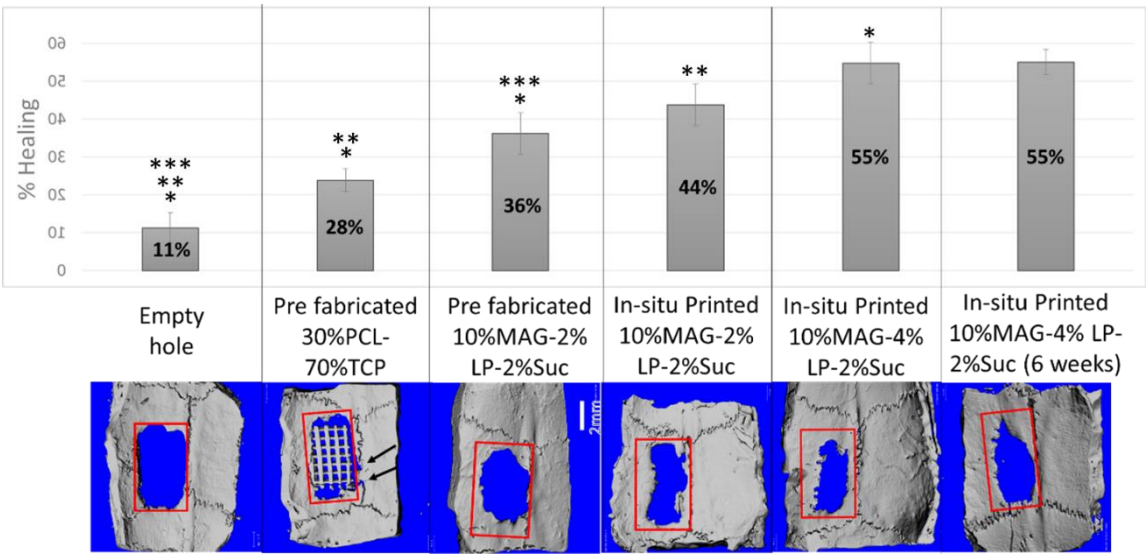

Figure 11. Micro-CT images from six different treatments and their corresponded healing percentage (n=3). The best healed sample of each group are selected for this figure.

2.3.6. Raman Spectroscopy

Raman spectroscopy showed that bio-ink had two characteristic bands of sucrose and sharp hydroxyproline peaks (Figure 12) that were not found in any region of the calvarial bones. Moving from fibrous tissue in the middle of the bone defect toward surrounding bone, PO_4 band intensity increases and also PO_4 band intensity relative to amide peaks increased in a similar fashion (Figure 12). Finally, Raman spectrum of the regenerated mineral is identical to surrounding endogenous bone.

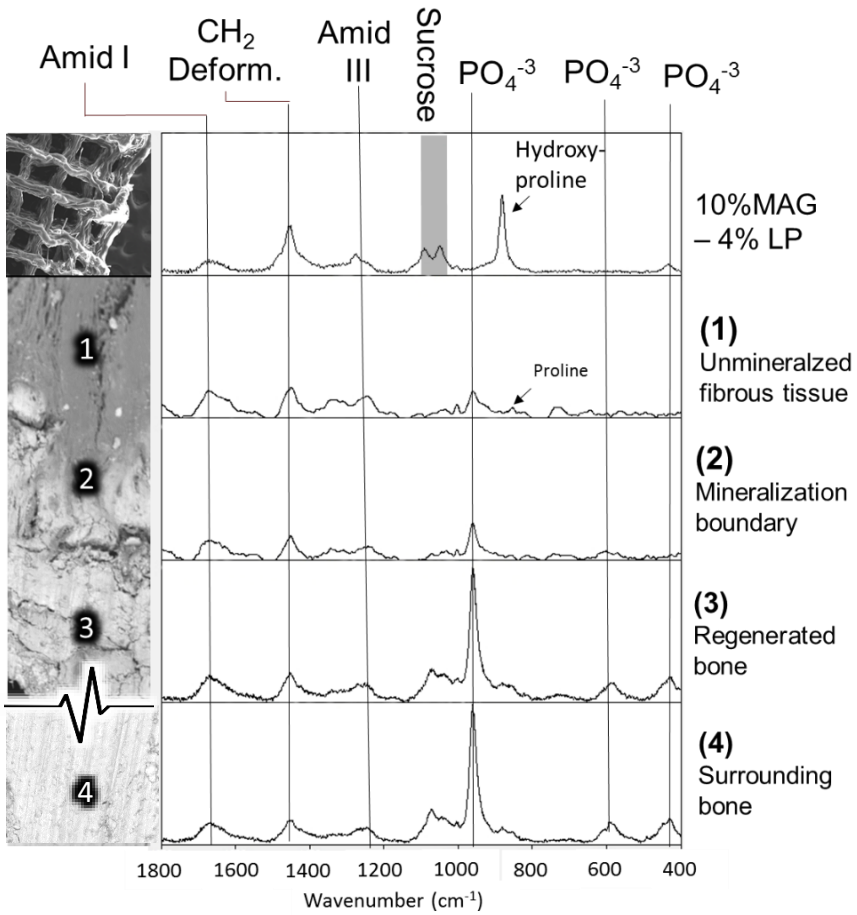

Figure 12. Raman Spectroscopy from the crosslinked 4-10 scaffolds and four different regions around RMF. The approximate spot of analysis on dissected bone is shown in a SEM image to the left.

2.3.7. Histology

Histological analysis of the rat's native bone (Figure 13) shows organized lamellae and parallel collagen bundles in the matrix. Also, vessels and a narrow diploe are visible.

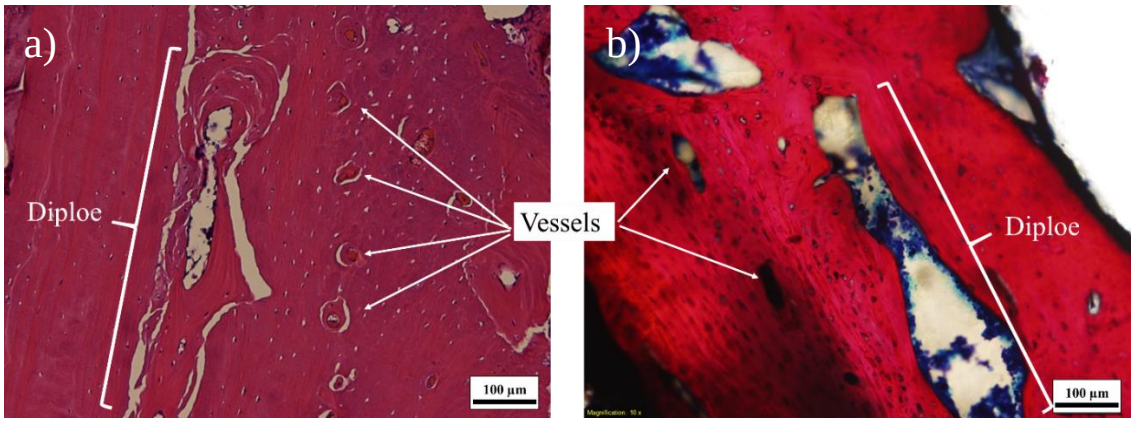

Figure 13. Section from a coronal plane of the defect stained with (a) H&E and (b) stevenel's blue. This image was taken from a calvarium of a rat dissected 4 weeks after in-situ printing of the 4-10 bio-ink. These slides show SB or rat's native bone. Organized collagen fibers, blood vessels, and diploe are characteristics of this region.

Two different type of regenerated bone was seen in RMF; they were either surrounded by fibrous tissue (Figure 14) or attached to surrounding bone (SB) (Figure 15). Purple color at the edge of the regenerated bone (RB) (white arrow in Figure 14) is hypo mineralized bone.

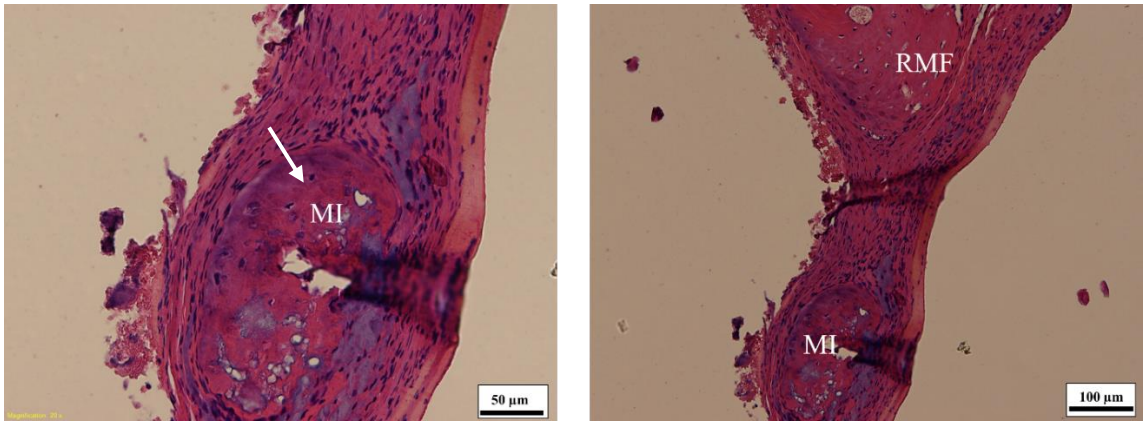

Figure 14. H&E stained section from a coronal plane of the defect. This image was taken from a calvarium of a rat dissected 4 weeks after in-situ printing of the 4-10 bio-ink. A distinct mineral isle (MI) is visible in the defect.

Newly regenerated bone is accompanied by vascularization. Some vessels are seen in the RB region (Figure 15 and Figure 16). Note that collagen fibers in these new RBs are randomly oriented and do not have a distinct lamellae structure, a characteristic of woven bone.

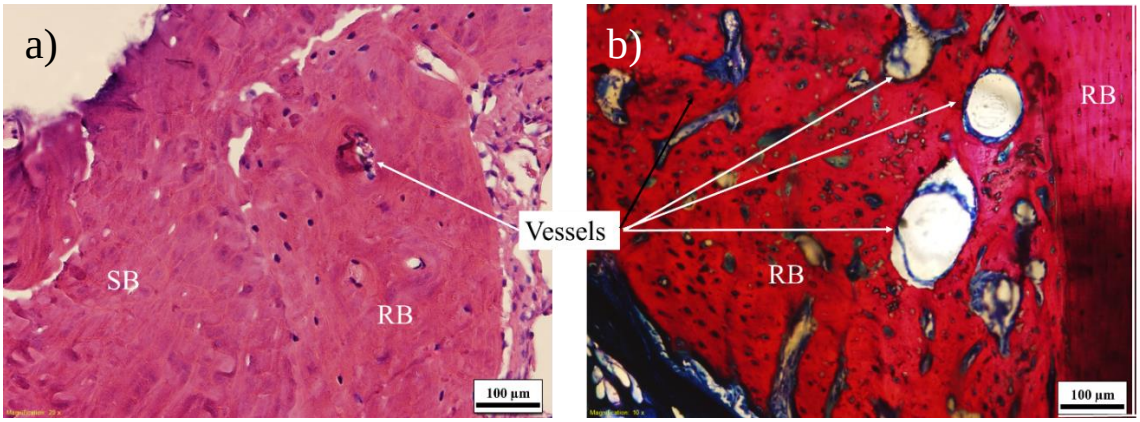

Figure 15. Section from a coronal plane of the defect stained with (a) H&E and (b) stevenel's blue. This image was taken from a calvarium of a rat dissected 4 weeks after in-situ printing of the 4-10 bio-ink. In some areas, RB was continuous with SB, suggesting that these bone are regenerated by proliferation and migration of osteoblasts rather than differentiation of stemcells.

Figure 16 shows signs of burnt bone and empty lacunae. Burnt bone was the result of heat generated by drilling during partial calvaria removal. The generated heat also killed osteocytes in the SB and essentially killed the peripheral bone. As a result, the rat's body isolated the dead tissue with a fibrous capsule.

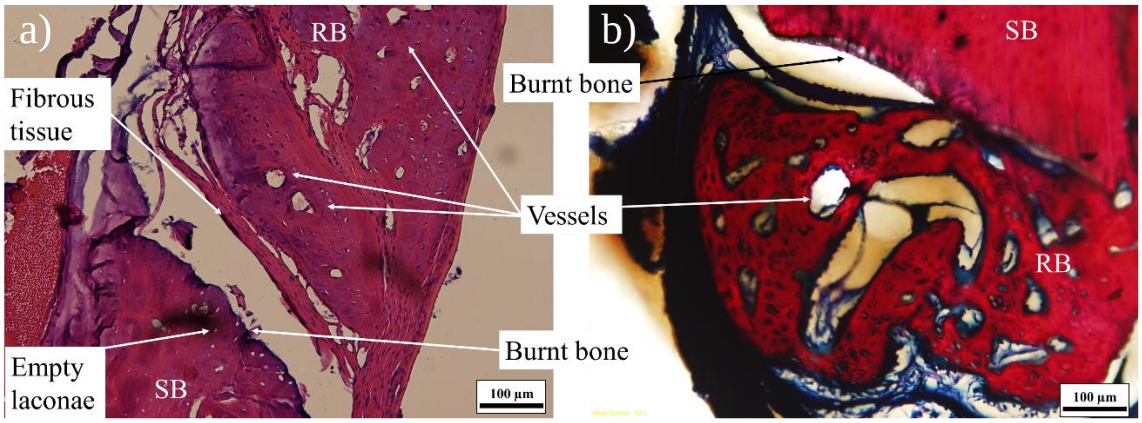

Figure 16. Section from a coronal plane of the defect stained with (a) H&E and (b) stevenel's blue. This image was taken from a calvarium of a rat dissected 4 weeks after in-situ printing of the 4-10 bio-ink. Vascularized regenerated bone (RB) is isolated from surrounding bone (SB) by a fibrous capsule. Cutting bone by high-speed dental burr generated enough heat to burn the bone and kill osteocytes (empty lacunae).

2.4. Discussion

In this study, we tested the hypothesis that incorporating sucrose into photo-crosslinkable gelatin silicate nanocomposite can make it suitable for in-situ 3DP. Our goal was to demonstrate that ISP technique can be used to regenerate bone similar to the body's native bone without any infection our chronic inflammation.

FTIR used for confirmation of successful methacrylation reaction. The results showed that amide peak in MAG compare to gelatin shifted toward higher wavenumbers. This shift is a characteristic of methacrylated gelatin [99-101] and could possibly be attributed to methacrylation reaction that converts gelatin's amino groups to an amide group. In this addition reaction, the methacrylate group of MA was added to the amino group on the gelatin chain. In MA molecule, the carbon of –C=O replaced by a proton of the amino group ($–NH_3$) and consequently, an amide bond was created (Figure 3.b). This newly formed amide group has a slightly different energy level due to

interaction with adjacent groups. This different energy level could possibly affect amide's peak in FTIR spectrum and shift the peak toward higher wavenumber. In MAG's FTIR spectrum, a shoulder near amide I peak was visible (near 1645cm^{-1}). This shoulder could be attributed to C=C of the grafted methacrylate group. There is no sign of the shoulder in the crosslinked bio-ink spectrum because the crosslinking initiated by opening of C=C bonds, and C=C does not exist in the composite anymore. Therefore, all these FTIR results confirm successful methacrylation of gelatin.

In the section 2.2.3, it is shown that incorporation of sucrose in the MAG-LP nanocomposite improved printability. This results could be related to two factors. First, cracks in extruded filaments that sometimes led to filament rupture. These cracks are attributed to the weak shear strength of hydrogel's filaments [102]. Hydrogels behave like solid materials and can resist shear stress [103]. In robocasting, extruded filament exhibits an aggressive bending force in order to change its direction from vertical to horizontal. Gelatin hydrogel cannot tolerate this force and breaks. The second factor that interrupts MAG-LP printability is the compressibility of the hydrogel under pressure [104]. Compressibility prevents a uniform extrusion of bio-ink from the tip of the dispenser. Also, under the compressed situation, maintaining a constant pressure in the barrel is challenging, considering that the pressure gradually built up as the printing starts and gradually drops as printing finishes. Gradual increase in pressure causes defected print in first few layers and a fluctuation in extrusion speed afterward. Also, the remained pressure causes the materials to keep flowing out even after the print finished. Sucrose reduced filament cracking, segmentation, and compressibility by interrupting

gelation. Sucrose prevent gelation by staying between gelatin polymer chains and intervening their interactions.

The printing speed which gave the best result was lower than what was calculated using (Equation 1). The calculated printing speed is 14.75 mm/minute for a plunger speed of 0.3 mm/minute while to best printings achieved at the speed of 9 mm/minute. The reason for this difference could be due to not considering effects of friction, viscosity, and compression in the formula. This formula works when there is no friction, viscosity's resistance, and material compression involve. However, as mentioned previously, hydrogels tend to become compressed in respond to pressure. Also, the synergistic effect of viscosity and friction during extrusion can affect the result [105]. The ratio of tube cross section area to extrusion cross section area has a reverse relationship with squared extrusion force. In other words, if the cross-sectional area of the extruded shape drops to half (when tube cross section area is constant), the required pressure will be quadrupled to allow the extrusion to occur [105]. This pressure is required to overcome the friction force between the material and the tube's surface. If the friction is too high, the pressure inside the tube will overcome viscosity before being able to overcome friction and the materials away from friction forces will start to move toward extrusion tip and extrude out [105]. That means when friction is high, extrusion rate is a function of viscosity. In this study, since the dispenser needle that is used for ISP has an inner diameter of only 0.2 millimeters (nearly 50 times smaller than tube's inner diameter), a considerably high friction is involved. Thus, viscosity force controls the extrusion speed. That phenomenon also explains the reason that the optimum

printing speed for the 6-20 bio-ink is slower than others (6 mm/minute). The optimum "dispenser to substrate" distance was found to be 0.05 mm less than the filament's diameter. This difference provides the extruded filament a better grip to the substrate and gives the best printing.

The minimum UV light intensity necessary for the cross-linking process at the printer speed of 9 mm/min, is determined to be 31 mW/cm2. However, higher intensity can also be used. 365nm UV light fall into UV-A category. UV-A lights are fairly safe and non-mutagenic [106]. The ACGIH minimum exposure recommendation is 1.0 J/cm2 for periods lasting less than 1000 seconds [106]. In ISP with a printing speed of 9 mm/min, UV exposure is around 1 second. Therefore, 31 mW/cm2 is considerably lower than maximum safe exposure at 365nm. However, it is always recommended to use the lowest possible irradiation. Therefore, UV light (wavelength: 365nm) with the intensity of 31.5 mW/cm^2 used as a standard for all printing. Note that UV exposed homogeneously throughout the entire sample since UV illumination was occurring while the material was extruded out from the dispenser. This fact also was also noticeable from the uniformity of scaffolds crosslinked by intensities above 31.5 mW/cm^2. Minimum thickness required for crosslinking depends on many factors, including the ability of the material to scatter light [107]. For MAG-LP nanocomposites, it was found that UV light with intensity as low as 6.9 mW/cm^2 can successfully crosslink a film with a thickness of 0.4 mm. Therefore, crosslinking in ISP method is expected to be uniform throughout the entire filament as the filament had a thickness of only < 0.2 mm.

BSE-SEM and histological images from remineralization front (RMF) revealed that two mechanisms are involved in remineralization. The first mechanism starts with nucleation of minerals near RMF. These mineral spots later grow and combine with each other and create mineral isles (MI). Afterward, mineral isles merge into RMF and healing continues. The second mechanism that was noted involves simple diffusion of mineral components into the unmineralized tissue. This diffusion probably is a result of cell migration into the defect from RMF and can suggest an active process of osteoconduction.

Raman spectroscopy results showed that PO_4 band intensity increases from unmineralized area in the center of the defect toward SB. This shows mineral content increased in this direction which is similar to what was found in SEM images and histological analysis. Bone maturity which is determined by the peak intensity ratio of PO_4 to amide band [86] also increase in a similar fashion (from the center of the defect to the SB). This finding is similar to what was observed in histological sections that show areas of hypomineralization at the edge of RB.

EDS analysis detected calcium and phosphorous in the healed area, whereas no calcium and phosphorus were detected in the bio-ink scaffold. This observation indicates that the source for this newly formed Ca and P is something other than the scaffold, perhaps the rat's body. Considering the fact that Raman data showed the presence of phosphorus in a form of PO_4, the detected Ca in EDS could be a part of the structure in coordination with PO_4. This structure can possibly be a newly formed calcium phosphate or HA.

Raman data from regenerated mineral (that contained Ca and PO_4) and SB revealed that these two regions have identical Raman spectrum. This result provides evidence that regenerated mineral is actually bone with the same chemistry and elements coordination as rat's native bone. All these findings match with the ossification process previously discussed in section 1.2 and shows that healing process in the presence of bio-ink occurred according to normal physiological bone healing.

EDS data revealed that there was no trace of Si element in both fibrous areas and RB. However, EDS taken from scaffold showed a detectable amount of Si in its matrix. This finding suggests there is no sign of scaffold in the defect and probably the scaffold is completely degraded before dissecting the calvaria (scaffold degraded before 4 weeks). Raman and histological analysis also confirm this finding. Raman analysis showed that two distinct bands of bio-ink (sucrose and hydroxyl proline) are not present in any region of the calvarial bone defect; also, no sign of MAG or LP was found in histological sections.

Histology images display the presence of vessels in the RB. The presence of vessels in RB can make it possible for newly developed bone to grow and become thicker since nutrients and oxygen are available to them. In fact, vascularization in RB help enhances healing rate specifically in CSDs [108, 109]. Reduced diploe and thick cortical bones on both sides of the calvarium are characteristics of rat's bone at this age (one year old). No inflammation or infection at healing sites was observed. However, there were some signs of foreign body reaction at RMF. These reactions were in respond to burnt bone at dissection boundaries. Dead bone encapsulation possibly compromised

osteoconduction and nutrient transfer to the defect. Therefore healing process in these areas was only possible through osteoinduction and the only way for nutrient and oxygen transfer was through the dura which could possibly slowed down the healing rate.

μCT results showed that there was a subtle increase in healing comparing conventional implantation of the scaffold and in-situ printing. However, these data are not statistically significant. μCT results also revealed that implantation of the scaffold with a higher concentration of LP (4-10) resulted in a faster healing compared to the pre-fabricated 2-10. This observation can show the effect of LP concentration on enhancing bone healing rate and supports previous findings about the role of LP in osteogenesis [78-81, 110, 111]. Also, the empty hole had significantly lower healing than pre-fabricated and in-situ printed bio-ink ($P<0.05$). This finding suggests that regardless of technique, bio-ink has the potential to enhance bone healing in CSD. No statistical difference in healing rate between the pre-fabricated 2-10 and the ISP 2-10 was found. Yet, low power of the study prevents us from ruling out the advantage of ISP in bone healing rate. Although the power of the study for the omnibus ANOVA analysis is > 99%, this high power could be due to the presence of empty hole and PCL-TCP treatment. Without considering those two treatments, the study power drops to 38% and also no statistical differences were found between groups. Too many groups in ISP trials and a few replicates per each group weakened the power of the study. However, it would have a better result if the number of groups was reduced and the number of replicates increased. With fewer groups and more replicates the power is expected to increase and provide more in-depth understanding of in-vivo aspects of ISP. Note that even if there

were no actual differences between the healing rate of the pre-fabricated 2-10 and the ISP 2-10, it would not rule out the advantages of using ISP for craniofacial reconstruction, since this method is devised to address delays in fabrication and precision in implantation.

Our data for the first aim show a potential in ISP compatible Bio-ink composite and in-situ printing technique for being used in healing CSDs. We introduced a practical way to combine fabrication and implantation of micropatterned scaffolds and possibly eliminate delay in fabrication, improve implantation precision and provide the capacity to modify scaffold's shape during surgery. However, to achieve more controlled degradation and better understanding the role of MAG and LP on physical properties of bio-ink, a cell-free degradation test, swelling test, and protein release with a high statistical power could be beneficial.

CHAPTER III

THE EFFECT OF LP AND MAG ON PHYSICAL PROPERTIES OF BIO-INK

3.1. Introduction

In chapter II, it is shown that by incorporating sucrose to an already established polymer nanosilicate, an ISP compatible material (bio-ink) was created. It is also shown that the in-situ printing concept is practical.

In this chapter, it is tried to understand the physical behavior of bio-ink and the role of its main components in this behavior. Since in the previous chapter, printed scaffold resorbed faster than bone healed, here, evaluating the mechanism of degradation in bio-ink is the main focus.

It is hypothesized that degradation rate, swelling rate, and protein release of bio-ink can be adjusted by controlling LP and MAG concentration.

As was mentioned previously, implant integration has two steps; bony union between the surface of the implant and native bone segments, and then graft remodeling and resorption in coordination with new bone formation [46]. Graft remodeling is defined as dynamic scaffold degradation and resorption in coordination with new bone formation. This is a critical step; degradation faster than bone formation will cause scaffold loosening and eventually leads to scaffold resorption before the defect heals. On the other hand, a degradation slower than the bone formation is not desirable and can

slow the healing process. Therefore, an adjusted degradation rate is needed to optimize the healing rate.

A big challenge in using gelatin hydrogel scaffolds is how to keep scaffold shape and micropatterning intact after fabrication [112]. Fabrication of gelatin-based 3D scaffolds are labor intensive and do not provide precise control over architecture due to high percentage of water in the hydrogels [113]. These hydrogels have the tendency to dehydrate in dry and swell in humid environments [83]. Both of these conditions will damage hydrogel scaffold's shape and precision which makes its manufacturing and handling hard and expensive. An advantage of the ISP technique is that there is no need for handling scaffolds. Also, its fabrication is easier and more precise than current conventional methods. However, the humid environment of the body can still causes the scaffold to swell. Thus, limiting swelling rate can be useful and improve bio-ink scaffold's precision. A swelling test can provide information about the effect of LP and MAG on the swelling rate of the bio-ink and how to control it.

MAG scaffolds have the ability to absorb water and water soluble molecules. Therefore, in the biological environment, they absorb blood, serum, and in general water soluble proteins. Protein release studies can evaluate the ability of scaffold to release already absorbed blood and serum proteins into the peripheral environment. These factors can contribute to enhancing the healing process. These experiments can also demonstrate the capability of the scaffold to carry and release a drug into the defect.

3.2. Materials and Methods

3.2.1. Scaffolds Compositions

Scaffold compositions that used in this study are according to Table 6. The total weight shows the amount of bio-ink prepared in each process. Note that this is the minimum recommended weight to prepare. Below these number, mixing process may not yield a homogeneous composite using the mentioned method.

Table 6. The composition of each bio-ink used in this thesis.

	6-20	**6-15**	**6-10**	**4-10**	**2-10**	**0-10**
Lp (gr)	0.3	0.3	0.3	0.2	0.1	0
Suc (gr)	0.2	0.15	0.1	0.1	0.1	0.1
I2959 (gr)	0.044	0.033	0.022	0.022	0.022	0.022
MAG (gr)	1	0.75	0.5	0.5	0.5	0.5
PBS (gr)	4	4.25	4.5	4.5	4.5	4.5
total (gr)	5.544	5.483	5.422	5.322	5.222	5.122

3.2.2. Sterilization Using Ethanol

All scaffolds not used for in-situ printing purposes went through another sterilization process after printing. The current robocaster 3D printer used for this study does not have an isolated and sterile environment. Therefore, there is a chance of scaffold contamination during and after printing. To prevent any unwanted parameter in tests, scaffolds went under another round of sterilization. Yet this time, EtO cannot be used since it requires a desiccation step that can cause dehydration and deformation in the bio-ink. As a result, 70% ethanol was used for scaffolds sterilization [114].

Scaffolds were incubated in well-plates filled with 4ml of 70% ethanol over a night followed by UV irradiation. Then, they were transferred to new well-plates and soaked in 4ml PBS twice, each time for two hours. Later on, they were immersed in 4ml α-MEM for 2 more hours. Finally, they transferred to new well-plate and were ready for a test.

3.2.3. Swelling Test

Gelatin hydrogels have the tendency to absorb water and proteins. In general, they tend to absorb any polar solvent or solute [83]. As a result of this absorption, they swell in a humid environments and release moisture in a dry environments. This phenomenon changes the shape of the scaffold and causes swelling and shrinkage respectively. Biological environments are a wet environment and can cause hydrogel scaffolds to swell. Therefore studying the swelling rate of bio-ink in exposure to a wet environment is necessary.

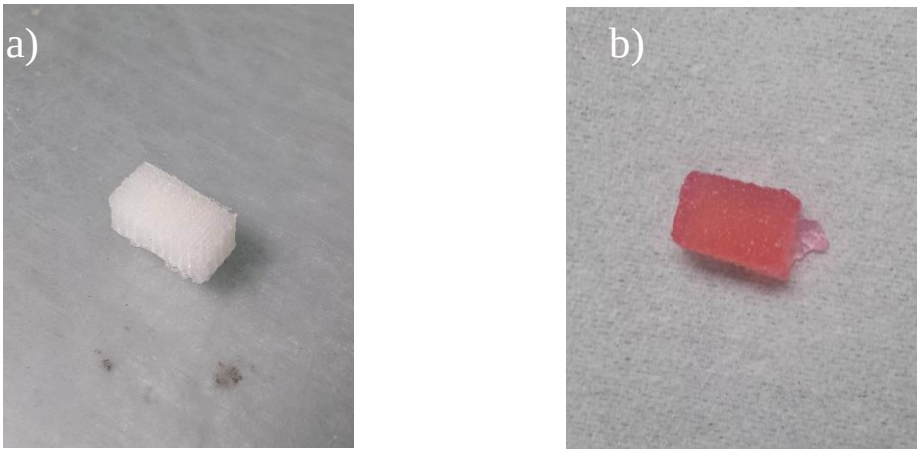

Figure 17. A scaffold of 6-20 before (a) and after (b) immersion in a growth medium. Growth medium contain phenol red that has a red color at 7.2 pH.

Scaffolds in dimensions of 9 x 6 x 2 mm were printing and weighed subsequently (W_d). Later, they were immersed in α-MEM (Life Technologies, Grand Island, NY) at 37°c for an hour. Afterward, scaffolds were removed from the medium, their surface dried by a filter paper, and they were weighed again (W_w). the percentage swelling was calculated using the following equation:

$$\%\, Swelling\ = \frac{W_w - W_d}{W_w} \times 100 \qquad \text{Equation 2}$$

Three different compositions of the 0-10, 6-10, and 6-20 scaffolds were prepared according to concentrations mentioned in Table 6. These compositions used to determine the effect of LP and MAG on swelling and four samples per each group were prepared. The 0-10 scaffolds served as a control for pure MAG, the comparison of this bio-ink with 6-10 can show the effect of LP in the swelling rate. Swelling was expressed as mean ± SD.

3.2.4. Protein Release Assay

To track the release of protein from the matrix of crosslinked gelatin, fluorescent labeled proteins were added to scaffolds. These labeled proteins are easy to track and distinguish from the gelatin of the scaffold (since MAG is not labeled). There are many different types of fluorescent dyes in the market, but fluorescein is one of the most popular labels for proteins [115]. Also among fluorescein labeled proteins, fluorescein isothiocyanate conjugated bovine serum albumin (FITC-BSA) is a well-established protein for drug delivery [115-117].

For this test, 0.1 %wt. FITC-BSA (A9771 SIGMA) was added to bio-inks of the 0-10, 6-10, and 6-20 scaffolds to determine the effect of LP and MAG on protein release

rate. Scaffolds with dimensions of 9 x 6 x 2 mm were printed and used. Eight samples per each group were designated and each sample was immersed into 2ml of the degradation media and stored at $37^{\circ c}$ for a week. Degradation media was selected for the in-vitro environment to observe protein release behavior of bio-ink resulting from both diffusion and enzymatic degradation.

Samples were collected at 4 hours, 1 day, 4 days, and 7 days. At each time point, a 50µL sample was collected from the medium in each well and replaced by 50µL fresh medium. All samples were then assayed at 488nm using UV-Vis spectroscopy. The FITC-BSA concentrations were calculated from absorbance using a calibration curve. Swelling ratio was expressed as mean±SD.

To graph the calibration curve, a set of media with known concentrations of FITC-BSA was prepared according to Table 7 (n=3). The absorbance of these media was measured at 488nm. Based on achieved absorbance, a graph of concentration vs. absorbance was generated. The relation between absorbance and concentration was achieved by a linear regression and used to calculate unknown concentration of FITC-BSA in the supernatant.

Table 7. Diluted media used for generating the standard curve. Stock media of 1mg/mL FITC-BSA in degradation media was used for the standard curve. Degradation media was used for dilution

Dilution	**stock**	**1:1**	**1:3**	**1:7**	**1:15**	**1:31**	**1:63**	**1:127**	**1:255**	**1:511**	**1:1023**	**1:2047**
Conc. Of FITC-BSA (mg/mL)	1	0.5000	0.25	0.125	0.0625	0.0313	0.0157	0.0079	0.004	0.002	0.001	0.0005

3.2.5. Cell-Free Degradation Test

To sustain remineralization and maturation of bone, the ability of the scaffold to degrade and remodel in a biological environment is crucial. Degradation rate is important and should be almost similar to bone healing rate of the host to always keep in contact with the defect periphery and support cell migration [46, 118]. A slow degradation rate should lead to slow healing rate. A cell-free degradation test is a comparative test to study the speed of degeneration of scaffolds and the effect of each ingredient of on the rate of degradation. This test was performed according to previous studies on cell-free degradation of gelatin-based scaffolds [119-121]. For this test two different media were prepared; 1% Pen-Strep in α-MEM was prepared to investigate only hydrolytic degradation rate, and 1 %vol. penicillin and streptomycin mixture (Pen-Strep) and 2U/ml Collagenase type II in α-MEM (degradation media) to evaluate enzymatic degradation. The presence of calcium for active functioning of collagenase is necessary. In other words, calcium is a cofactor of collagenase [122]. Collagenase units (U) are defined as a concentration that cleaves peptides of collagen of bovine Achilles tendon to 1.0 μmole of leucine in 5 hours at pH 7.4 and 37 °C [123].

Scaffolds with dimensions of 4 x 6 x 4 mm in six different compositions were printed, weighed, and immersed into 3ml of medium. Six different compositions of the 0-10, 2-10, 4-10, 6-10, 6-15, 6-20 scaffolds were used for the study and four samples were designated per each group. At 1, 2, 5, 7, 10, and 14 days time points, 50μL media were collected from each specimen's supernatant and replaced by 50μL fresh medium. Collected media was analyzed for leached ions using inductively coupled plasma optical

emission spectrometry (ICP-OES). At the end of the test, samples were removed (if they were still present in the media), freeze-dried and weighed again. Degradation rate was determined by comparing the adjusted change in weight of each scaffold at the end of the test.

3.3. Results

3.3.1. Swelling Test

All scaffolds exhibited an increase in weight when they were immersed in the alpha-MEM solution (Figure 18). The highest swelling rate belongs to bio-ink without LP with 19.7 ± 2.08 % swelling which was significantly ($P < 0.05$) higher than all other samples (Table 8).

Table 8. % swelling of bio-ink with different compositions after immersion in alpha-MEM

0-10			**6-10**			**6-20**		
W_d **(gr)**	W_w **(gr)**	**% swelling**	W_d **(gr)**	W_w **(gr)**	**% swelling**	W_d **(gr)**	W_w **(gr)**	**% swelling**
0.16	0.188	17.5	0.146	0.159	8.90411	0.159	0.179	12.57862
0.158	0.194	22.78481	0.131	0.143	9.160305	0.153	0.173	13.0719
0.161	0.199	23.60248	0.15	0.162	8	0.152	0.172	13.15789
0.16	0.184	15	0.141	0.148	4.964539	0.153	0.17	11.11111
	Average:	19.72182		**Average:**	7.757238		**Average:**	12.47988
	SE	2.075121		**SE**	0.963588		**SE**	0.473767

The statistical power of the study was 41% which is too low to claim there is no statistical difference between the 6-10 and 6-20.

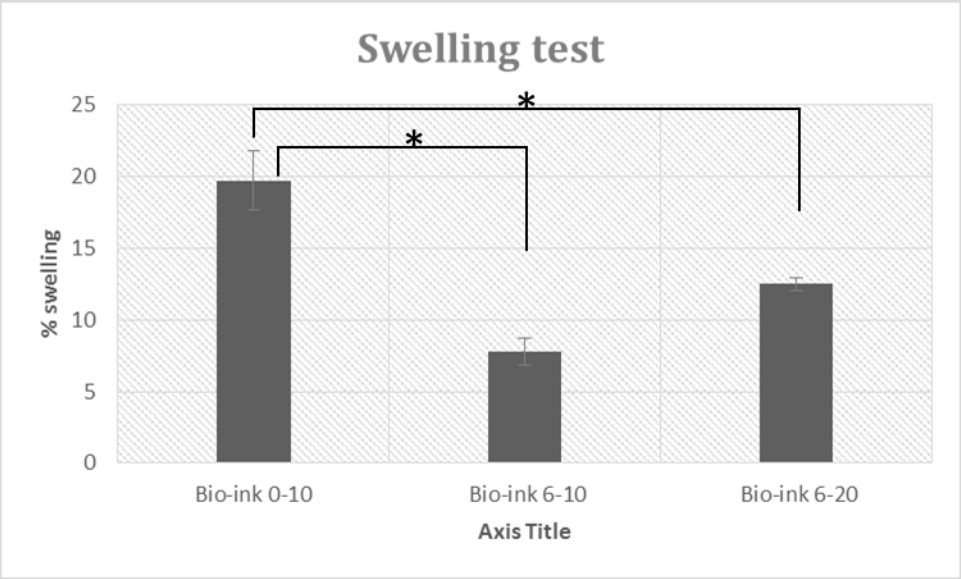

Figure 18. % swelling of different compositions of bio-ink, showing the effect of LP and MAG on degradation (n=4). * Data is not parametric. Therefore Kruskal-Wallis one-way Analysis of Variance on Ranks with Tukey correction was performed ($P<0.05$)

3.3.2. Protein Release Assay

A standard curve was generated for the assay. This curve was generated by diluting known concentrations of FITC-BSA in alpha-MEM. The concentration of FITC-BCA has a linear relationship with absorption at 488nm (Figure 19). This relation follows the formula:

$$\text{Conc.} = (0.3307 \pm 0.003)\,(\text{Abs}) + (0.0226 \pm 0.003),\ R^2 = 0.9992 \qquad \text{Equation 3}$$

Using this formula, FITC-BSA concentration in supernatants were calculated.

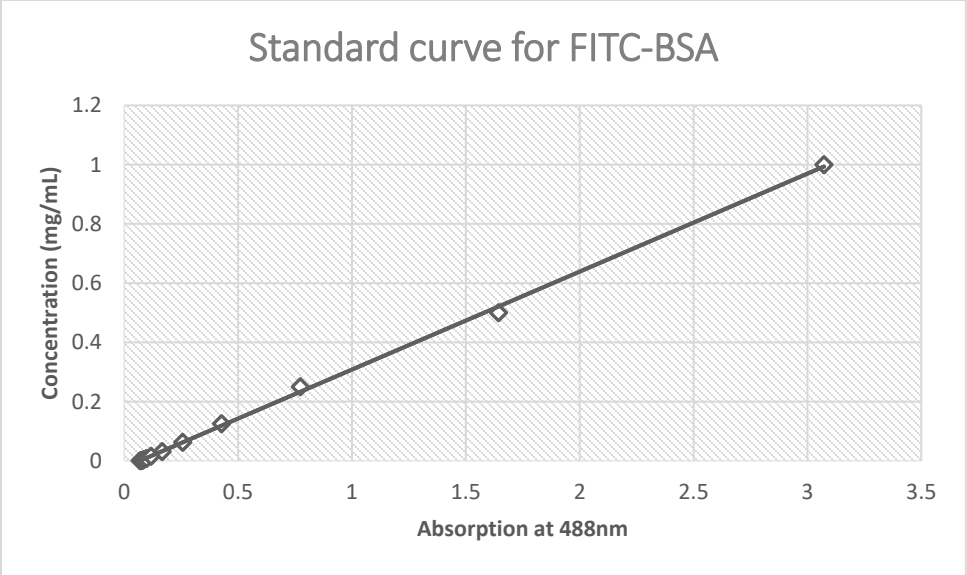

Figure 19. Standard curve created for evaluating FITC-BSA concentration in the supernatant. It shows that concentration of FITC-BSA has a linear relation with absorption at 488nm that follows the equation conc. = 0.3307 (Abs) – 0.0226 (n=3)

Release studies showed that scaffolds from the different groups had similar behavior at 4 hours of study (Figure 20). However, protein release for the 0-10 scaffolds increased from day 1 and continued until day 4. At this point, the scaffold was completely dissolved. The maximum concentration of FITC-BSA measured in the media was 0.055 g/mL.

The results showed that all groups behaved significantly different than the others ($P < 0.05$). 6-10 showed the lowest release of FITC-BSA among all types of scaffolds and the 6-20 scaffolds had an intermediate release rate.

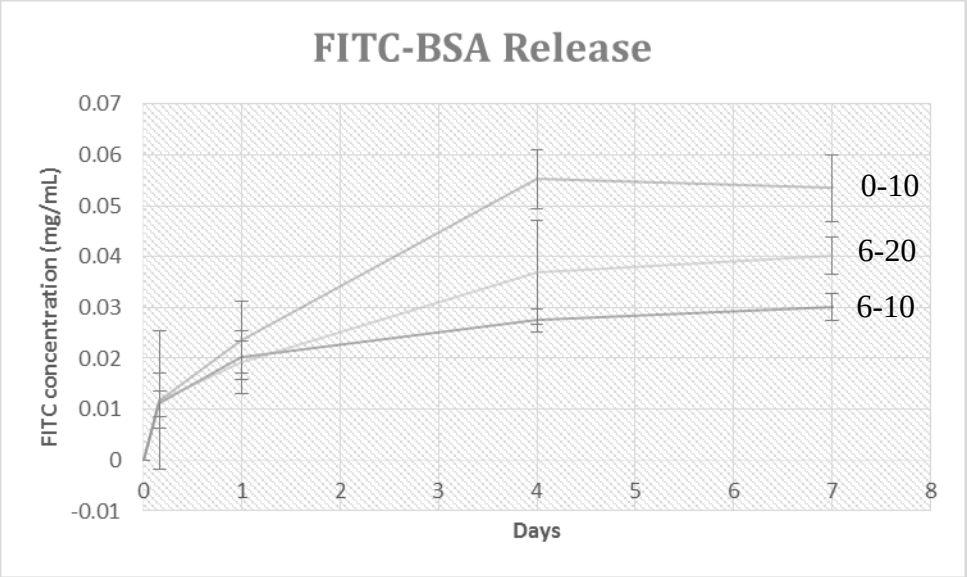

Figure 20. FITC-BSA concentration release pattern. Samples collected after 4 hours, 1 day, 4 days, 7 days (n=8). These concentrations are calculated using standard curve (Figure 19. Standard curve created for evaluating FITC-BSA concentration in the supernatant. It shows that concentration of FITC-BSA has a linear relation with absorption at 488nm that follows the equation).
* All groups are significantly different from each other.

3.3.3. Cell-Free Degradation

In the cell-free degradation study, 6 different compositions of scaffold in two different media (w/ collagenase and w/o collagenase) were tested. Visual changes of the samples in degradation test is shown in Figure 21. In degradation media (with collagenase), the 2-10, and 4-10 scaffolds were completely degraded in less than a day. Interestingly, the scaffolds in 0-10 group did not completely degraded and only become smaller. At day 5, the 0-10 scaffolds samples were completely degraded. At day 7, the 6-10 scaffold started to disintegrate into small pieces Figure 21. Interestingly, the pattern of degradation for 6-10 was totally different from what was observed for the 0-10 scaffolds. No notable changes in samples gross appearance were observed from day 7 until the end of the study (14 days) except disintegration and degradation of 6-10

scaffolds. The degradation test in alpha-MEM (without collagenase) showed that none of the scaffolds exhibited any notable changes in their gross appearance in two weeks of study.

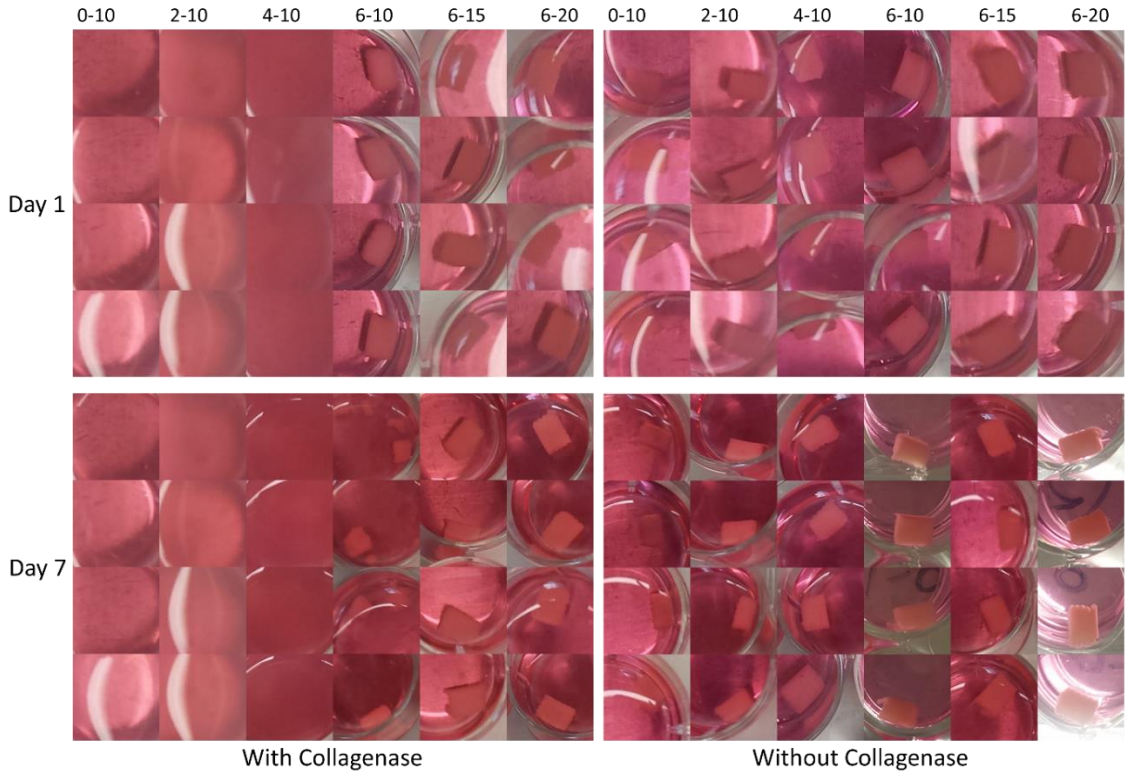

Figure 21. The gross appearance of the scaffolds in degradation media with and without collagenase. The length of the degradation study was 14 days. However, after day 7 there were no notable changes in any of the samples gross appearance except the 6-10 samples that continue disintegrating and degrading.

Two weeks after immersing samples into the both media, all samples were taken out, lyophilized, and weighed (D_{14}). To compare degradation among different groups, the scaffolds' lyophilized weights were compared to the adjusted dry weight of the samples at day zero (lyophilized right after printing). Day zero dry weights were adjusted because samples did not have same exact weight after printing. Considering that

dried samples are light in weight, the weight difference after printing between the degradation study samples and day zero samples (which are different scaffolds) could introduce artifact and error into the analysis. To adjust the difference, the average weight reduction after lyophilization was measured for day zero samples of each composition. This average was termed “day zero constant” and showed the average weight reduction of each type of bio-ink if they were lyophilized right after printing (day zero). To determine “day zero constant” 8 samples per each group were used (n=8).

$$Day\ zero\ constant = \frac{\sum_{group}(\frac{W_w - W_d}{W_w} \times 100)}{n} \quad \text{Equation 4}$$

Where W_w is Day zero samples weight after printing and W_d Day zero samples weight after freeze-drying. This constant was used on the degradation study samples to evaluate their dry weight if they were lyophilized after printing:

$$D_0 = d_0\ X\ (Day\ zero\ constant) \quad \text{Equation 5}$$

Where D_0 is adjusted degradation study samples dry weight after printing and d_0 is degradation study samples dry weight after printing. Afterward, the adjusted degradation rate was measured by the following formula:

$$\%weight\ change = \frac{D_0 - D_{14}}{D_0} \times 100 \quad \text{Equation 6}$$

Where D_0 is adjusted degradation study samples dry weight after printing and D_{14} is degradation study samples weight after 14 days.

The degradation study in alpha-MEM showed no weight change in the 0-10 group (the actual mean of weight change was -1.002%) and the highest weight loss was

belong to the 2-10 scaffolds and then the 4-10 scaffolds (Figure 22). None of the other groups had significant differences in degradation. The power of the study is > 99%.

In collagenase media, the 6-20 scaffolds showed the least weight loss followed by the 6-15 scaffolds. The 6-10 scaffolds exhibited more than 85% weight loss and other compositions (0-10, 2-10, 4-10) degraded completely after 14 days.

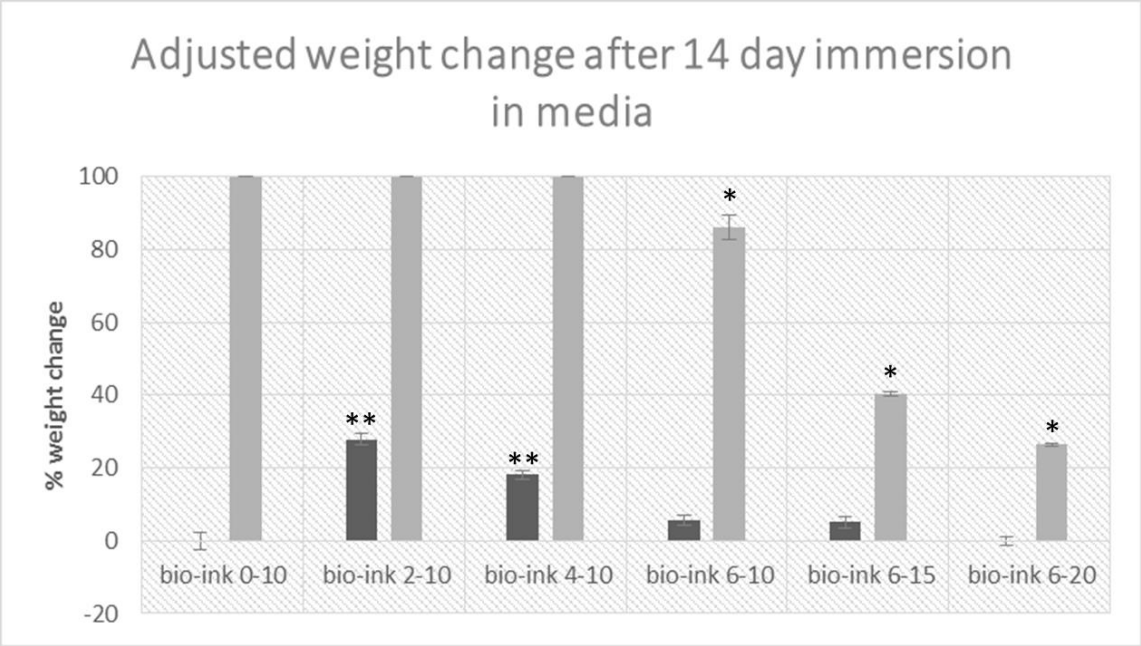

Figure 22. Adjusted weight changes of scaffolds after 14 days immersion in the media. (n=4).
* In degradation test with degradation media, all groups' means are significantly different except the 0-10, 2-10, and 4-10 scaffolds. ($P < 0.001$). ** In degradation test in alpha-MEM, the 2-10 and 4-10 scaffolds were significantly different from other groups.

3.4. Discussion

Bio-ink swelling decreased by increasing LP concentration and conversely increased by increasing MAG. It can possibly shows that water diffusion into the hydrogel is regulated by the concentration of LP. The reason for this phenomenon could be related to the entangled structure of LP-MAG complex. As was discussed in section

2.2.3, this microstructure interaction with MAG polymer chains creates an entangled and rigid structure (Figure 2). At low LP concentration, its nanoplatelets surface completely covered by MAG. Increasing LP will provide more sites of attachment for gelatin and increases the ionic interaction between LP and MAG which results in a more rigid structure [124]. Rigid structure provides less flexibility for the hydrogel network which makes it harder for water molecules to penetrate. Hence, the scaffold's water absorption decreases. On the other hand, the addition of more MAG to the bio-ink will introduce more free-MAG (not in interaction with LP) in the matrix. These free chains can readily absorb water and consequently swell. In other words, network strength is regulated by LP and the swelling rate depends on the MAG to LP ratio.

Data from the protein release studies indicates that all three types of bio-inks (0-10, 6-10, 6-20) exhibited a burst release initially and the release rate dropped gradually. When area close to the surface of scaffold released their FITC-BSA, continuation of the release depends on diffusion of FITC-BSA from the core of scaffold to the surface. Reduction in release rate implies that release (diffusion) of FITC-BSA from the surface to the media is faster than diffusion of FITC-BSA within the scaffold. In other words, the protein release is limited to diffusion of FITC-BSA within the scaffold [125]. Note that the media contained collagenase. Therefore, some of FITC-BSA molecule release is due to gelatin degradation rather than diffusion. As was shown in section 3.3.3, enzymatic degradation of gelatin occurred from the surface. Mladenovska K et al also reported the same pattern of enzymatic degradation of gelatin [126]. As the scaffold degrades, it gets smaller and its surface area reduces. Reduction of surface area reduces

available sites for enzymatic degradation. Thus, this phenomenon also can contribute to the reduction in release rate of FITC-BSA as a function of time.

The lowest protein release rate belonged to the 6-10 group. This result was expected due to the prediction of the LP and MAG interaction. Since MAG to LP ratio is the lowest in the 6-10 scaffolds, it has the strongest network of all groups. While strong networks resist water diffusion, they would not let the trapped molecules escape either [127].

In the protein release study, the average weight of a 0-10 scaffold printed was 140 mg. At this weight, scaffolds contained about 140 µg FITC-BSA. If the whole scaffold dissolves in 2 mL media (which happened in this study), the concentration of FITC-BSA should be 70 µg/mL. This difference could be because of some burst release while scaffold was being washed (after printing and before immersion). Also, more importantly, replacement of 50 µL of media with a fresh one at each time point gradually diluted it. It also explains the drop in concentration after 4 days for the 0-10 scaffolds. Since the scaffold is completely degraded no more FITC-BSA was released and collecting a sample only diluted the supernatant.

The degradation study reveals that hydrolytic degradation plays a small role in MAG degradation. It is slow enough that no weight loss was detectable at 2 weeks in the 0-10 scaffolds. By this time, the 2-10 scaffolds had the most weight loss. The reason for this weight loss could be a release of LP into the media considering that MAG is not subjected to degradation in two weeks. The 2-10 scaffolds have a low concentration of both LP and MAG and a considerably higher water portion which resulted in a weaker

microstructure. In this weak microstructure LP can release into the media easier [127]. The 4-10 scaffolds are probably suffered from the same issues. Therefore, a collagenase-free environment probably provides a situation in which LP release is controlled by diffusion [124]. Other scaffolds (6-10, 6-15, and 6-20) have strong enough microstructure that significantly slowed down the release of LP [127]. Inductively coupled plasma optical emission spectrometry (ICP-OES) is a very precise technique to measure ion concentration in a media. This technique can reveal more in-depth information about LP release rate. Thus, it is highly recommended to investigate this theory using ICP-OES.

Enzymatic environments are more similar to the in-vivo situation in a way that cells in the body use different proteases to break down collagen fibers and matrix to remodel them [128]. Therefore studying degradation in collagenase media can provide more realistic results for scaffold degradation rate and factors affecting them. Results from the degradation study using collagenase media showed that as gelatin concentration increased, scaffold's weight loss was reduced so scaffolds with low MAG such as the 0-10, 2-10, 4-10 scaffolds are completely degraded and the 6-10 scaffolds lost a significant portion of its mass. This observation suggests that enzymatic degradation possibly is controlled by gelatin concentration [119, 120, 129]. The reason that the 6-10 scaffolds showed a slower degradation rate relative to the 0-10, 2-10, and 4-10 scaffolds, could be due to its high LP concentration. Overall, increased LP concentration will reduce degradation rate of hydrogels [130] relative to other bio-inks with lower LP. This high LP concentration can possibly halt the release of gelatin's by-products and trap them in a

locally created thixotropic gel [131]. In other words, this gel makes it harder for collagenase to access the inner network of gelatin. This phenomenon could explain the reason that the 6-10 scaffolds degradation pattern was different from that of the 0-10, 2-10, and 4-10 scaffolds. Those disintegrated pieces of the 6-10 scaffolds were actually local thixotropic gels that held gelatin by-products together. This theory is strengthen when it was observed that lyophilized remnants of the 6-10 scaffols were powder instead of pieces of scaffolds. The 6-20 scaffolds showed the least weight loss followed by the 6-15 scaffolds.

These tests provide a more in-depth understanding of bio-ink and the role of LP and MAG on bio-ink physical behavior. To summarize, it was shown that an increase in LP and/or MAG concentration reduces degradation rate. However, MAG concentration plays a bigger role in enzymatic degradation. In other words, MAG concentration controlled enzymatic degradation. Furthermore, an increase in LP concentration reduces protein release and swelling rate, while an increase in MAG concentration increases protein release and swelling rate.

CHAPTER IV

FUTURE WORKS AND CONCLUSION

4.1. Introduction

This study showed that the ISP concept is practical and can induce bone healing similar to current conventional implantation methods without having notable toxicity, infection or prolonged inflammation. In addition, due to its capacity to combine fabrication and implantation, it can potentially eliminate problems that may arise from the delay in surgery due to the time needed for custom implant fabrication and also a mismatch between the scaffold and the defect.

These features can be useful for scaffold implantation after tumor dissection, congenital deformities correction, etc. In-situ printing also can potentially reduce the risk of damaging the tissue during fabrication/implantation, by precisely control its probe movements. This feature is extremely important specifically for craniofacial reconstruction that deals with bones in areas proximal to vital tissues.

This thesis proves that by increasing LP and MAG concentration, degradation rate significantly reduces. However, it is not clear what would be the effect of these changes on biological properties of bio-ink. To propose an optimum concentration for bio-ink, a set of in-vitro studies is required to understand the effect of MAG and LP on cell toxicity, attachment, proliferation, migration, and differentiation. Performing all these tests is out of the scope of this master thesis and is planned to be done in future.

In this chapter, cells' migration on bio-ink's surface was studies. The results of this study serves as the preliminary data for future works.

4.2. Materials and Methods

4.2.1. Cell Migration and Attachment

A key characteristics of an ideal scaffold is to enhance cells' migration and attachment. Therefore, the capacity of different bio-ink compositions to facilitate cells' migration and attachment was evaluated. For this study, scaffolds with dimensions of 6 x 12 x 1.5 mm were printed. Three different compositions of the 0-10, 6-10, and 6-20 hydrogels were used for the study and 6 replicates were designated for each composition. PDPCs were seeded on one side of each scaffold's top surface. On each scaffold approximately 25,000 cells were seeded. A week after seeding, scaffolds were fixed and stained by Hoechst and Phalloidin immunohistochemical dyes. Immunofluorescence microscopy images were obtained using a Large Fields Fluorescence Stereo Zoom Microscope (Axio Zoom.V16, ZEISS, US).

Periosteum derived progenitor cells (PDPCs) have several advantages for bone regeneration in-vitro studies. A minimal invasion is needed to harvest these cells. PDPCs can keep their differentiation capacities through many passages (usually P5) and also grow fast [132]. They maintain their growth curve for more than thirty doubling [133] and would not become senescence until around eighty doubling. PDPC's growth would not be inhibited by contacting each other, and they continue to proliferate into higher densities [134, 135]. PDPCs have the capacity to differentiate into osteogenic,

chondrogenic, and adipogenic lineages [136]. Harvested PDPCs from old individuals also keep their growth potential but lose the capacity to differentiate into chondrocytes and adipocytes [137]. Furthermore, PDPCs regenerate bone de novo and have osteoinductive effects [138]. Also, reagents to induce in-vitro differentiation in PDPCs are well-established. All these factors make PDPCs ideal for regenerative tissue engineering and a more accurate clinical translation [136].

PDPC were obtained according to IRB protocol (Study ID STU 012011-181) as previously described [139]. These cells (passage 2) were cultured in 75cm^2 flasks with growth media in a humidified atmosphere of 95% air and 5% CO2 at 37$^{\circ c}$ and incubated for a week. The media was changed every two days to keep the growth condition optimum and also prevent any potential contamination. Growth media was an α-MEM based media contained 10% fetal bovine serum or FBS (VWR, Radnor, PA), and 1% streptomycin and penicillin or Pen-Strep (HyClone, 10,000 unit/ml) as an antibiotic.

A week after plating, cells were trypsinized (T4049 SIGMA) and counted. Cell concentration was adjusted to 2,750,000 cells/ml and 20µL of the cell media (25,000 cells) was used for seeding (passage 3). Cells were seeded on scaffolds inside 12-wells plates. Cells were tried to be seeded only on one side of the scaffold in order to analyze cells' migration. However, due to the hydrophilic surface of bio-ink, in many samples cell media spread all over the scaffold once they were seeded.

Cell culture media is a solution that can provide essential inorganic and organic components that cells need for growth. It has three main component of "Minimum Essential Media" or (MEM), a blood serum, and an antibiotic.

The minimum essential media (MEM) contains essential inorganic salts, amino acids, vitamins, and sugars for cell viability. It also has a buffer and pH indicator such as phenol red to keeping the track of pH. There are many different types of MEM such as Eagle's MEM, Dulbecco's modified Eagle's Medium (D-MEM), and alpha-modified minimum essential media (α-MEM). Each is designed for different application and cell line. For our study, α-MEM (gibco by life technologies^{tm}) was the suitable MEM [125] and used for the entire study.

The serum contained proteins, vitamins, hormones, and growth factors required for cell viability and growth. The penicillin and streptomycin antibiotic also added to growth media to eliminate any bacterial growth in case of contamination.

Cells immunohistochemical staining technique was used to stain cells' nuclei and actin filament. By staining those two, studying the osteoblasts adhesion, migration, and proliferation can be visualized and analyzed using fluorescent microscopy and image processing techniques.

The blue-fluorescent Hoechst dyes are nucleic acid stains that are sensitive to DNA conformation and chromatin. These bisbenzimidazole derivatives are supravital stains that bind to the minor groove of DNA. The dye's fluorescence will be enhanced two times more by binding to AT-rich dsDNA regions versus GC-rich strands. For that reason, Hoechst can be used for many different applications from flow cytometric recognition of DNA damage [140] to cell counting [141]. The advantages of Hoechst over DAPI staining for cell counting application is that Hoechst is cell permeable and non-toxic which makes it a more efficient dye. For this study Hoechst 33342,

trihydrochloride, trihydrate, (H3570, Invitrogen, US) with absorption at 405 and emission at 440-500nm was used.

Phallotoxins are toxins that are isolated from Amanita phalloides mushrooms. These toxins can bind competitively to F-actin. Therefore, by labeling the toxin with a Fluorescent dye, the amount of F-actin in cells can be quantified under a fluorescent microscope [142]. For this study Alexa Fluor® 488 Phalloidin (A12379, Invitrogen, ThermoFisher scientific) is used that excites at 488nm and emit at 500nm-650nm.

To prepare samples, cells were fixed by adding 2ml of 4% PFA to each well for 10 min and washing twice with PBS. Then, samples were permeabilized by immersing them in absolute acetone at −20°C for 2–3 minutes. Afterward, the acetone was diluted gradually with cold PBS. Later on, hydrogels incubated in PBS with 1%BSA for more efficient staining. After aspirating BSA solution, nuclei stained by incubating samples in a Hoechst solution of 2µg/ml for 15 min and washing twice with PBS. F-actin stained by incubating the samples with 200 µL of 0.33 µM Phalloidin for 30 minutes and then washing twice with PBS. The whole process of staining was done in a dark area to prevent bleaching of the dyes.

4.3. Results

4.3.1. Cell Migration and Attachment

A week after incubating the seeded 0-10 scaffolds, PDPCs spread on the surface. After proliferation on the seeded spot, they immigrated and colonized unseeded areas of

samples. Their stretched filopodia (Figure 23) shows that the sample's surface is cellophil and cells were in the process of migration.

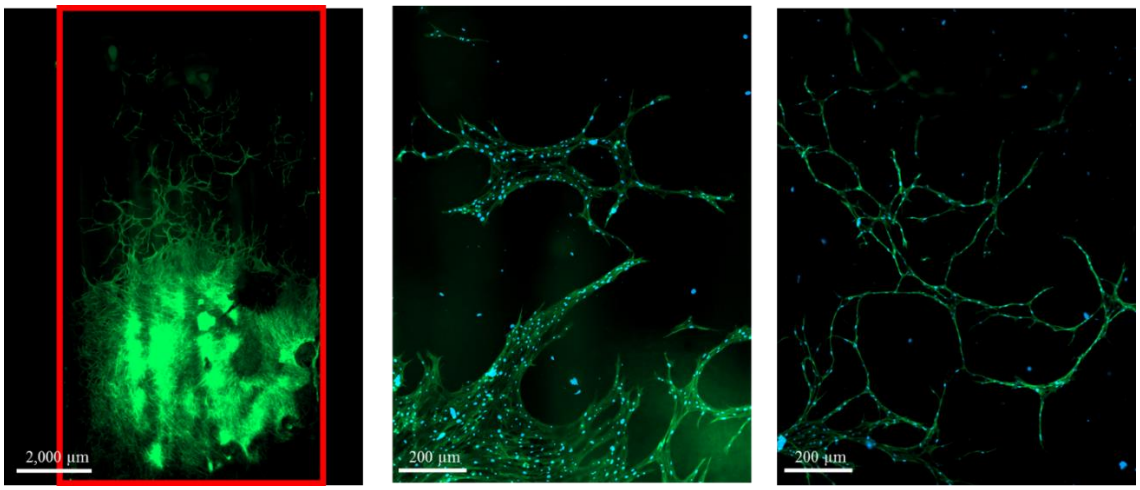

Figure 23. Immunohistochemistry images from human PDPCs on bio-inks of the 0-10 scaffolds. Blue color represents cell's nucleus and green color represents cell's F-actin. Cells were seeded on the bottom side of each scaffold and incubated for one week. The red box shows the scaffold boundaries.

On the 6-10 scaffolds, very few cells survived and those survived had rounded shapes (Figure 24). Cells can only be found in seeded region and did not migrate to other areas of the scaffold. No clear filopodia and lamellipodia were detected.

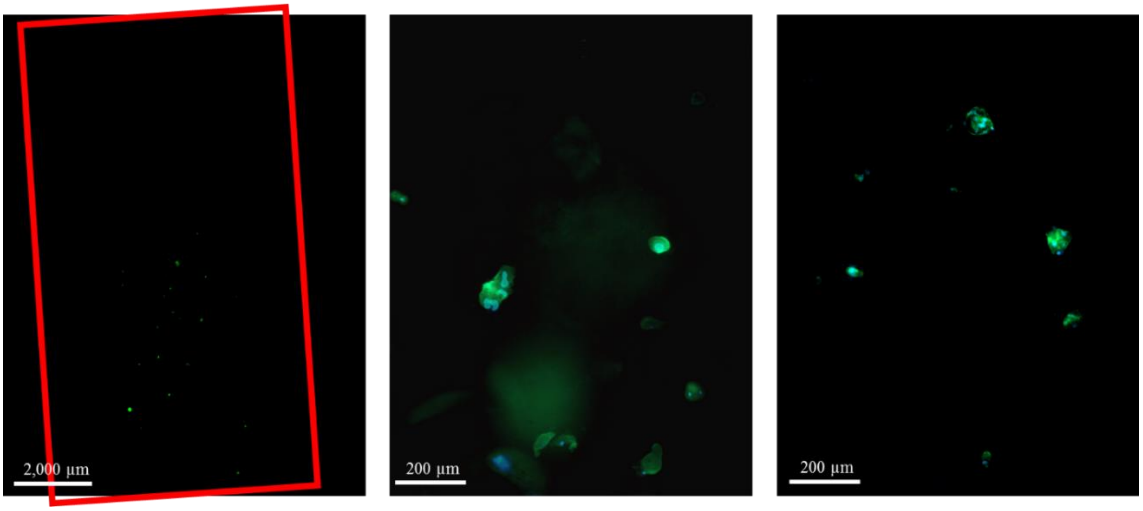

Figure 24. Immunohistochemistry images from human PDPCs on bio-inks of 6-10. Blue color represents cell's nucleus and green color represents cell's F-actin. Cells were seeded on the bottom side of each scaffold and incubated for one week. The red box shows the scaffold's boundaries.

Fluorescent microscope images from 6-20 scaffolds showed colonies of cells on the scaffold (Figure 25). although the covered area by cells on the 6-20 hydrogels is smaller than the covered area on the 0-10, it is much bigger than the covered area on the 6-10 hydrogels. In high magnification, some stretched filopodia and lamellipodia are evident. Furthermore, presence of the colonies outside the seeding area, indicating that the cells were able to migrate. Moreover, microscope images show the cells colonies in different planes; considering that scaffold's surface is relatively flat, colonies in different planes can indicate that cells were penetrated into the scaffold.

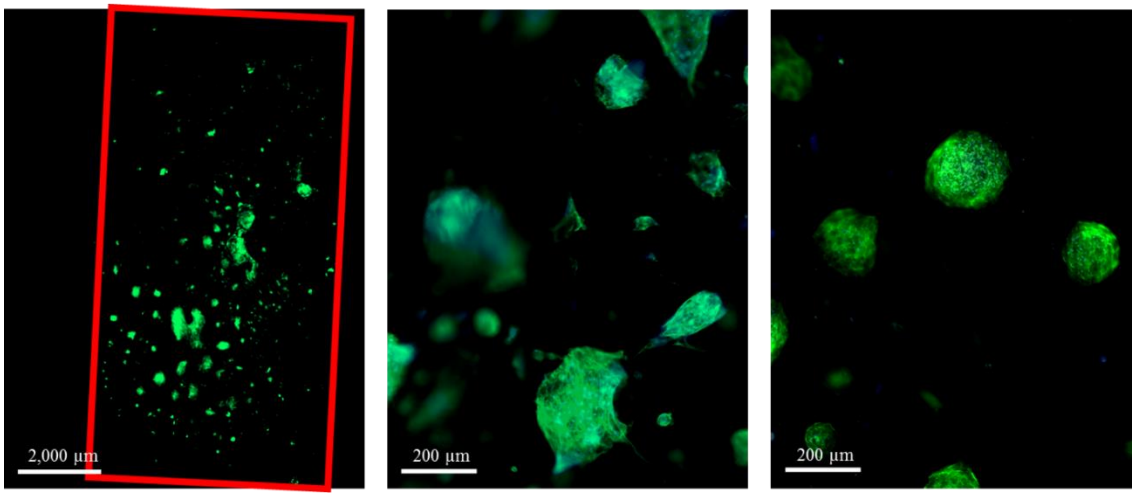

Figure 25. Immunohistochemistry images from human PDPCs on bio-inks of 6-20. Blue color represents cell's nucleus and green color represents cell's F-actin. Cells were seeded on the bottom side of each scaffold and incubated for one week. The red box shows the scaffold's boundaries.

4.4. Discussion

Immunohistochemistry staining showed cells reaction to the surface of the 0-10, 6-10, and 6-20 bio-inks. Overall, cells on the 0-10 hydrogels were stretched (fibrillar adhesions) and connected with filopodia and also moved from seeding area to cover the scaffold. These observations indicate that the surface of the 0-10 hydrogels enhanced cells attachment and facilitate their migration [114, 143]. On the other hand, rounded shape of cells on the 6-10 hydrogels shows that cells did not attach well to its surface. Low cell count also indicates its toxicity to cells. It is shown that a high concentration of LP could be toxic to cells. Previously, Gaharwar et al. showed that LP concentration above 1 mg/mL in the media can be toxic to cells [80]. At those concentrations, LP nanodisks engulf cells and limit cells functionality. Also, LP nanoplatelets can electrostatically bind to proteins in the media and make them inaccessible for cells. Therefore, LP release should be limited.

Cells arrangement on the 6-20 hydrogela under the fluorescent microscope (Figure 25) shows a higher count of cells relative to the 6-10 hydrogels with more stretched morphology. Cells colonies outside seeding area were also noted. These findings reveal that cell's attachment, migration, and growth are improved on the 6-20 compared to 6-10 hydrogels. However, cells still struggle reaching their maximum attachment and growth. It can be indicated that the toxicity a scaffold with a high level of LP can be reduced by increase MAG concentration. In addition, cells attachment can be restored in a similar way. This improvement in cell attachment can be due to a reduction in LP release rate in a similar way as we saw in 3.3.3. A control on LP release is possible through two distinct ways, by reducing LP concentration or by increasing MAG and trapping LP particles inside the matrix. The first option can limit overall LP release however it would not fix the LP burst release that was seen in degradation study (Figure 22). As a result, the initial burst in LP release still can damage cells. An increase in MAG concentration besides limiting LP release can provide more binding sites (RGD motifs) for cells and consequently enhances cell's attachment.

This thesis proved that by increasing LP and MAG concentration, degradation rate significantly reduces. However, it comes with a tradeoff; high concentration of LP is toxic to cells. Like other drugs, LP can be toxic if it exceeds its toxic dosage. This study failed to propose an optimum composition for bio-ink. However, a strong relation between bio-ink's components and its physical and biological properties is established.

In future, different compositions will be tested in-vitro to find the optimum composition of bio-ink for ISP application. The author suggests studying 4-20 or 5-25

which have high gelatin portion to control LP release, enhance cells attachment and possibly reduce degradation rate. Also using MTT assay can help understanding bio-ink's toxicity. In later stages, investigation of cell differentiation would also be beneficial.

REFERENCES

[1] Vacanti CA. The history of tissue engineering. Journal of Cellular and Molecular Medicine 2006;10:569-76.

[2] Langer R, Vacanti JP. Tissue engineering. Science 1993;260:920-6.

[3] Sipe JD. Tissue Engineering and Reparative Medicine. Annals of the New York Academy of Sciences 2002;961:1-9.

[4] Langer R, Vacanti J. Tissue engineering. Science 1993;260:920-6.

[5] Saxena S, Ray AR, Kapil A, Pavon-Djavid G, Letourneur D, Gupta B, et al. Development of a new polypropylene-based suture: plasma grafting, surface treatment, characterization, and biocompatibility studies. Macromolecular Bioscience 2011;11:373-82.

[6] Chapman MW. Chapman's orthopaedic surgery. Third ed. Philadelphia, PA: Lippincott Williams & Wilkins; 2001.

[7] Grundnes O, Reikeras O. The importance of the hematoma for fracture healing in rats. Acta Orthopaedica Scandinavica 1993;64:340-2.

[8] Glowacki J. Angiogenesis in fracture repair. Clinical Orthopaedics and Related Research 1998:S82-9.

[9] Bolander ME. Regulation of fracture repair by growth factors. Proceedings of the Society for Experimental Biology and Medicine Society for Experimental Biology and Medicine (New York, NY) 1992;200:165-70.

[10] McKibbin B. The biology of fracture healing in long bones. The Journal of Bone and Joint Surgery British volume 1978;60-b:150-62.

[11] Rockwood CA, Green DP, Bucholz RW. Rockwood & Green's fractures in adults. Seventh ed. Philadelphia, PA: Lippincott, Williams & Wilkins; 2010.

[12] Lieberman JR, Friedlaender GE. Bone regeneration and repair : biology and clinical applications. edited by Jay R. Lieberman and Gary E. Friedlander. Totowa, NJ: Humana Press; 2005.

[13] Arnett TR. Extracellular pH regulates bone cell function. The Journal of Nutrition 2008;138:415s-8s.

[14] Bord S, Horner A, Hembry RM, Reynolds JJ, Compston JE. Production of collagenase by human osteoblasts and osteoclasts in vivo. Bone 1996;19:35-40.

[15] Raggatt LJ, Partridge NC. Cellular and molecular mechanisms of bone remodeling. The Journal of Biological Chemistry 2010;285:25103-8.

[16] Shi D. Introduction to biomaterials. Beijing, China: Tsinghua University Press; 2006.

[17] Bronzino JD. The Biomedical engineering handbook. United States: CRC Press; 1995.

[18] Poitout DG. Biomechanics and Biomaterials in Orthopedics. London: Springer London; 2004.

[19] Williams DF. Essential biomaterials science. David Williams: Cambridge, United Kingdom ; New York : Cambridge University Press; 2014.

[20] Annabi N, Nichol JW, Zhong X, Ji C, Koshy S, Khademhosseini A, et al. Controlling the porosity and microarchitecture of hydrogels for tissue engineering. Tissue Engineering Part B, Reviews 2010;16:371-83.

[21] Brock A, Chang E, Ho CC, LeDuc P, Jiang X, Whitesides GM, et al. Geometric determinants of directional cell motility revealed using microcontact printing. Langmuir : the ACS journal of surfaces and colloids 2003;19:1611-7.

[22] Toyota T, Wakamoto Y, Hayashi K, Ohnuma K. Controlling cell migration with micropatterns. Agbo EC, editor. Innovations in Biotechnology: InTech; 2012.

[23] Sunami H, Yokota I, Igarashi Y. Influence of the pattern size of micropatterned scaffolds on cell morphology, proliferation, migration and F-actin expression. Biomaterials Science 2014;2:399-409.

[24] Yoon S-H, Kim YK, Han ED, Seo Y-H, Kim BH, Mofrad MRK. Passive control of cell locomotion using micropatterns: the effect of micropattern geometry on the migratory behavior of adherent cells. Lab on a Chip 2012;12:2391-402.

[25] Murphy CM, O'Brien FJ. Understanding the effect of mean pore size on cell activity in collagen-glycosaminoglycan scaffolds. Cell Adhesion & Migration 2010;4:377-81.

[26] Tarafder S, Balla VK, Davies NM, Bandyopadhyay A, Bose S. Microwave-sintered 3D printed tricalcium phosphate scaffolds for bone tissue engineering. Journal of Tissue Engineering and Regenerative Medicine 2013;7:631-41.

[27] Karageorgiou V, Kaplan D. Porosity of 3D biomaterial scaffolds and osteogenesis. Biomaterials 2005;26:5474-91.

[28] Xue W, Krishna BV, Bandyopadhyay A, Bose S. Processing and biocompatibility evaluation of laser processed porous titanium. Acta Biomaterialia 2007;3:1007-18.

[29] Otsuki B, Takemoto M, Fujibayashi S, Neo M, Kokubo T, Nakamura T. Pore throat size and connectivity determine bone and tissue ingrowth into porous implants: Three-dimensional micro-CT based structural analyses of porous bioactive titanium implants. Biomaterials 2006;27:5892-900.

[30] Bone Grafts and Substitutes Market (By Type: Allografts, and Bone Graft Substitutes; By Application: Spinal Fusion, Long Bone, Foot and Ankle, Craniomaxillofacial, Joint Reconstruction, and Dental) - Global Industry Analysis, Size, Share, Growth, Trends and Forecast 2015 - 2023. Transparency Market Research; 2016. p. 87.

[31] Bucholz RW. Nonallograft osteoconductive bone graft substitutes. Clinical Orthopaedics and Related Research 2002:44-52.

[32] Damien CJ, Parsons JR. Bone graft and bone graft substitutes: a review of current technology and applications. Journal of Applied Biomaterials 1991;2:187-208.

[33] Younger EM, Chapman MW. Morbidity at bone graft donor sites. Journal of Orthopaedic Trauma 1989;3:192-5.

[34] Panetta NJ, Gupta DM, Slater BJ, Kwan MD, Liu KJ, Longaker MT. Tissue engineering in cleft palate and other congenital malformations. Pediatric Research 2008;63:545-51.

[35] Oppenheimer AJ, Tong L, Buchman SR. Craniofacial bone grafting: wolff's law revisited. Craniomaxillofacial Trauma & Reconstruction 2008;1:49-61.

[36] McCarthy JG, Stelnicki EJ, Mehrara BJ, Longaker MT. Distraction osteogenesis of the craniofacial skeleton. Plastic and Reconstructive Surgery 2001;107:1812-27.

[37] Bell RB. Computer planning and intraoperative navigation in cranio-maxillofacial surgery. Oral and Maxillofacial Surgery Clinics of North America 2010;22:135-56.

[38] Hutmacher DW. Scaffolds in tissue engineering bone and cartilage. Biomaterials 2000;21:2529-43.

[39] Bose S, Vahabzadeh S, Bandyopadhyay A. Bone tissue engineering using 3D printing. Materials Today 2013;16:496-504.

[40] Cesarano III J, Calvert PD. Freeforming objects with low-binder slurry. Google Patents; 2000.

[41] Lewis JA, Smay JE, Stuecker J, Cesarano J. Direct ink writing of three-dimensional ceramic structures. Journal of the American Ceramic Society 2006;89:3599-609.

[42] Joshi AM. Process planning for the rapid machining of custom bone implants, Iowa, USA: Iowa State University; 2011.

[43] Beger HG. From archiv fur klinische chirurgie to langenbeck's archives of surgery: 1860-2010. Deutsche Gesellschaft fur Chirurgie 2010;395 Suppl 1:3-12.

[44] Wang W, Ouyang Y, Poh CK. Orthopaedic implant technology: biomaterials from past to future. Annals of the Academy of Medicine, Singapore 2011;40:237-44.

[45] Norowski PA, Jr., Bumgardner JD. Biomaterial and antibiotic strategies for peri-implantitis: a review. Journal of Biomedical Materials Research Part B, Applied biomaterials 2009;88:530-43.

[46] Bhumiratana S, Vunjak-Novakovic G. Concise review: rersonalized human bone grafts for reconstructing head and face. Stem Cells Translational Medicine 2012;1:64-9.

[47] Elsalanty ME, Genecov DG. Bone grafts in craniofacial surgery. Craniomaxillofac Trauma Reconstr 2009;2:125-34.

[48] Kokubo T, Kim HM, Kawashita M. Novel bioactive materials with different mechanical properties. Biomaterials 2003;24:2161-75.

[49] Guda T, Walker JA, Pollot BE, Appleford MR, Oh S, Ong JL, et al. In vivo performance of bilayer hydroxyapatite scaffolds for bone tissue regeneration in the rabbit radius. Journal of Materials Science Materials in Medicine 2011;22:647-56.

[50] Shih TC, Teng NC, Wang PD, Lin CT, Yang JC, Fong SW, et al. In vivo evaluation of resorbable bone graft substitutes in beagles: histological properties. Journal of Biomedical Materials Research Part A 2013;101:2405-11.

[51] Reffitt DM, Ogston N, Jugdaohsingh R, Cheung HFJ, Evans BAJ, Thompson RPH, et al. Orthosilicic acid stimulates collagen type 1 synthesis and osteoblastic differentiation in human osteoblast-like cells in vitro. Bone 2003;32:127-35.

[52] Varanasi VG, Saiz E, Loomer PM, Ancheta B, Uritani N, Ho SP, et al. Enhanced osteocalcin expression by osteoblast-like cells (MC3T3-E1) exposed to bioactive coating glass (SiO2-CaO-P2O5-MgO-K2O-Na2O system) ions. Acta Biomater 2009;5:3536-47.

[53] Varanasi VG, Owyoung JB, Saiz E, Marshall SJ, Marshall GW, Loomer PM. The ionic products of bioactive glass particle dissolution enhance periodontal ligament fibroblast osteocalcin expression and enhance early mineralized tissue development. Journal of Biomedical Materials Research Part A 2011;98A:177-84.

[54] Hoppe A, Guldal NS, Boccaccini AR. A review of the biological response to ionic dissolution products from bioactive glasses and glass-ceramics. Biomaterials 2011;32:2757-74.

[55] Maehira F, Iinuma Y, Eguchi Y, Miyagi I, Teruya S. Effects of soluble silicon compound and deep-sea water on biochemical and mechanical properties of bone and the related gene expression in mice. Journal of Bone and Mineral Metabolism 2008;26:446-55.

[56] Izu A, Kumai T, Tohno Y, Tohno S, Minami T, Yamada G, et al. Silicon intake to vertebral columns of mice after dietary supply. Biological Trace Element Research 2006;113:297-316.

[57] Rahaman MN, Day DE, Bal BS, Fu Q, Jung SB, Bonewald LF, et al. Bioactive glass in tissue engineering. Acta Biomater 2011;7:2355-73.

[58] Kobayashi H, Turner AS, Seim HB, 3rd, Kawamoto T, Bauer TW. Evaluation of a silica-containing bone graft substitute in a vertebral defect model. Journal of Biomedical Materials Research Part A 2010;92:596-603.

[59] Knapp CI, Feuille F, Cochran DL, Mellonig JT. Clinical and histologic evaluation of bone-replacement grafts in the treatment of localized alveolar ridge defects. Part 2: bioactive glass particulate. The International Journal of Periodontics & Restorative Dentistry 2003;23:129-37.

[60] Zhao S, Zhang J, Zhu M, Zhang Y, Liu Z, Tao C, et al. Three-dimensional printed strontium-containing mesoporous bioactive glass scaffolds for repairing rat critical-sized calvarial defects. Acta Biomaterialia 2015;12:270-80.

[61] Sui B, Zhong G, Sun J. Evolution of a mesoporous bioactive glass scaffold implanted in rat femur evaluated by 45Ca labeling, tracing, and histological analysis. ACS Applied Materials & Interfaces 2014;6:3528-35.

[62] Kretlow JD, Young S, Klouda L, Wong M, Mikos AG. Injectable biomaterials for regenerating complex craniofacial tissues. Advanced materials 2009;21:3368-93.

[63] Dunne M, Corrigan I, Ramtoola Z. Influence of particle size and dissolution conditions on the degradation properties of polylactide-co-glycolide particles. Biomaterials 2000;21:1659-68.

[64] Gentile P, Chiono V, Carmagnola I, Hatton PV. An overview of poly(lactic-co-glycolic) acid (PLGA)-based biomaterials for bone tissue engineering. International Journal of Molecular Sciences 2014;15:3640-59.

[65] Sanger C, Soto A, Mussa F, Sanzo M, Sardo L, Donati PA, et al. Maximizing

results in craniofacial surgery with bioresorbable fixation devices. The Journal of Craniofacial Surgery 2007;18:926-30.

[66] Fedorowicz Z, Nasser M, Newton JT, Oliver RJ. Resorbable versus titanium plates for orthognathic surgery. The Cochrane Database of Systematic Reviews 2007:Cd006204.

[67] Bell RB, Kindsfater CS. The use of biodegradable plates and screws to stabilize facial fractures. Journal of Oral and Maxillofacial Surgery : Official Journal of the American Association of Oral and Maxillofacial Surgeons 2006;64:31-9.

[68] Laughlin RM, Block MS, Wilk R, Malloy RB, Kent JN. Resorbable plates for the fixation of mandibular fractures: a prospective study. Journal of Oral and Maxillofacial surgery : Official Journal of the American Association of Oral and Maxillofacial Surgeons 2007;65:89-96.

[69] Kawasaki K, Aihara M, Honmo J, Sakurai S, Fujimaki Y, Sakamoto K, et al. Effects of recombinant human bone morphogenetic protein-2 on differentiation of cells isolated from human bone, muscle, and skin. Bone 1998;23:223-31.

[70] Meng ZX, Li HF, Sun ZZ, Zheng W, Zheng YF. Fabrication of mineralized electrospun PLGA and PLGA/gelatin nanofibers and their potential in bone tissue engineering. Materials Science & Engineering C, Materials for Biological Applications 2013;33:699-706.

[71] Ito Y. Covalently immobilized biosignal molecule materials for tissue engineering. Soft Matter 2008;4:46-56.

[72] Yoon JJ, Song SH, Lee DS, Park TG. Immobilization of cell adhesive RGD peptide onto the surface of highly porous biodegradable polymer scaffolds fabricated by a gas foaming/salt leaching method. Biomaterials 2004;25:5613-20.

[73] Pierschbacher MD, Ruoslahti E. Cell attachment activity of fibronectin can be duplicated by small synthetic fragments of the molecule. Nature 1984;309:30-3.

[74] Loth T, Hötzel R, Kascholke C, Anderegg U, Schulz-Siegmund M, Hacker MC. Gelatin-based biomaterial engineering with anhydride-containing oligomeric cross-linkers. Biomacromolecules 2014;15:2104-18.

[75] Nichol JW, Koshy ST, Bae H, Hwang CM, Yamanlar S, Khademhosseini A. Cell-laden microengineered gelatin methacrylate hydrogels. Biomaterials 2010;31:5536-44.

[76] Balazs AC, Emrick T, Russell TP. Nanoparticle polymer composites: where two small worlds meet. Science 2006;314:1107-10.

[77] Bordes P, Pollet E, Avérous L. Nano-biocomposites: biodegradable polyester/nanoclay systems. Progress in Polymer Science 2009;34:125-55.

[78] Xavier JR, Thakur T, Desai P, Jaiswal MK, Sears N, Cosgriff-Hernandez E, et al. Bioactive nanoengineered hydrogels for bone tissue engineering: A Growth-Factor-Free Approach. ACS Nano 2015.

[79] Wu C-J, Gaharwar AK, Schexnailder PJ, Schmidt G. Development of biomedical polymer-silicate nanocomposites: a materials science perspective. Materials 2010;3:2986-3005.

[80] Gaharwar AK, Mihaila SM, Swami A, Patel A, Sant S, Reis RL, et al. Bioactive silicate nanoplatelets for osteogenic differentiation of human mesenchymal stem cells. Advanced Materials 2013;25:3329-36.

[81] Dolatshahi-Pirouz A, Nikkhah M, Gaharwar AK, Hashmi B, Guermani E, Aliabadi H, et al. A combinatorial cell-laden gel microarray for inducing osteogenic differentiation of human mesenchymal stem cells. Scientific Reports 2014;4:3896.

[82] Thompson DW, Butterworth JT. The nature of laponite and its aqueous dispersions. Journal of Colloid and Interface Science 1992;151:236-43.

[83] Boral S, Gupta AN, Bohidar HB. Swelling and de-swelling kinetics of gelatin hydrogels in ethanol–water marginal solvent. International Journal of Biological Macromolecules 2006;39:240-9.

[84] Bouxsein ML, Boyd SK, Christiansen BA, Guldberg RE, Jepsen KJ, Muller R. Guidelines for assessment of bone microstructure in rodents using micro-computed tomography. Journal of Bone and Mineral Research : the Official Journal of the American Society for Bone and Mineral Research 2010;25:1468-86.

[85] Mandair GS, Morris MD. Contributions of Raman spectroscopy to the understanding of bone strength. BoneKey Rep 2015;4.

[86] Tarnowski CP, Ignelzi MA, Jr., Morris MD. Mineralization of developing mouse calvaria as revealed by Raman microspectroscopy. Journal of Bone and Mineral Research : The Official Journal of the American Society for Bone and Mineral Research 2002;17:1118-26.

[87] McElderry DP. Dynamics of Mineralization During Bone Development. Ann Arbor, MI: The University of Michigan; 2012.

[88] Al-Ruqaie IM, Kasapis S, Abeysekera R. Structural properties of pectin-gelatin gels. Part II effect of sucroseglucose syrup. Carbohydrate Polymers 1997;34:309-21.

[89] Nishinari K, Watase M, Kohyama K, Nishinari N, Oakenfull D, Koide S, et al. The effect of sucrose on the thermo-reversible gel-sol transition in agarose and gelatin. Polym J 1992;24:871-7.

[90] Weaver CM, Daniel JR. The Food Chemistry Laboratory: A manual for experimental foods, dietetics, and food scientists, Second Edition. USA: CRC Press 2003.

[91] Sabnis A, Rahimi M, Chapman C, Nguyen KT. Cytocompatibility studies of an in situ photopolymerized thermoresponsive hydrogel nanoparticle system using human aortic smooth muscle cells. Journal of Biomedical Materials Research Part A 2009;91:52-9.

[92] Loessner D, Meinert C, Kaemmerer E, Martine LC, Yue K, Levett PA, et al. Functionalization, preparation and use of cell-laden gelatin methacryloyl-based hydrogels as modular tissue culture platforms. Nat Protocols 2016;11:727-46.

[93] Normand V, Muller S, Ravey J-C, Parker A. Gelation kinetics of gelatin: a master curve and network modeling. Macromolecules 2000;33:1063-71.

[94] Patel RG, Purwada A, Cerchietti L, Inghirami G, Melnick A, Gaharwar AK, et al. Microscale bioadhesive hydrogel arrays for cell engineering applications. Cellular and Molecular Bioengineering 2014;7:394-408.

[95] Zandi M. Studies on the gelation of gelatin solutions and on the use of resulting gels for medical scaffolds. Essen, Germany: Universität Duisburg-Essen; 2008.

[96] Ilyas A, Odatsu T, Shah A, Monte F, Kim HKW, Kramer P, et al. Amorphous silica: a new antioxidant role for rapid critical-sized bone defect healing. Adv Healthcare Mater 2016.

[97] Shin H, Olsen BD, Khademhosseini A. The mechanical properties and cytotoxicity of cell-laden double-network hydrogels based on photocrosslinkable gelatin and gellan gum biomacromolecules. Biomaterials 2012;33:3143-52.

[98] Grill A. Porous pSiCOH ultralow-k dielectrics for chip interconnects prepared by PECVD. Annual Review of Materials Research 2009;39:49-69.

[99] Dragusin D-M, Van Vlierberghe S, Dubruel P, Dierick M, Van Hoorebeke L, Declercq HA, et al. Novel gelatin-PHEMA porous scaffolds for tissue engineering applications. Soft Matter 2012;8:9589-602.

[100] Wang H, Zhou L, Liao J, Tan Y, Ouyang K, Ning C, et al. Cell-laden photocrosslinked GelMA–DexMA copolymer hydrogels with tunable mechanical properties for tissue engineering. Journal of Materials Science: Materials in Medicine

2014;25:2173-83.

[101] Saraiva SM, Miguel SP, Ribeiro MP, Coutinho P, Correia IJ. Synthesis and characterization of a photocrosslinkable chitosan-gelatin hydrogel aimed for tissue regeneration. RSC Advances 2015;5:63478-88.

[102] Ferry JD. Viscoelastic properties of polymers: New York, NY: Wiley; 1961.

[103] Pierre AC. Introduction to Sol-Gel Processing. USA: Springer; 1998.

[104] Tan BH, Tan JPK, Tam KC. pH-responsive nanogels: synthesis and physical properties. hydrogel micro and nanoparticles : Wiley-VCH Verlag GmbH & Co. KGaA; 2012. p. 81-115.

[105] Saha PK. Aluminum Extrusion Technology. Ohio, USA: ASM International; 2000.

[106] American Conference of Governmental Industrial Hygienists. Documentation of the threshold limit values and biological exposure indices, 7th Edition. USA: ACGIH; 2015. p. 238.

[107] Anseth KS, Shastri VR, Langer R. Photopolymerizable degradable polyanhydrides with osteocompatibility. Nat Biotech 1999;17:156-9.

[108] Kini U, Nandeesh BN. Physiology of bone formation, remodeling, and metabolism. Fogelman I, Gnanasegaran G, van der Wall H, editors. Radionuclide and Hybrid Bone Imaging. Berlin, Heidelberg: Springer; 2012. p. 29-57.

[109] Rinaldi M, Esposti A, Mottola A, Ganz SD. Chapter 3 - Computer-assisted implant surgery. Computer-guided applications for dental implants, bone Grafting, and reconstructive surgery (Adapted Translation). St. Louis, MO: Elsevier; 2016. p. 96-123.

[110] Gaharwar AK, Mukundan S, Karaca E, Dolatshahi-Pirouz A, Patel A, Rangarajan K, et al. Nanoclay-enriched poly(varepsilon-caprolactone) electrospun scaffolds for osteogenic differentiation of human mesenchymal stem cells. Tissue Engineering Part A 2014;20:2088-101.

[111] Mihaila SM, Gaharwar AK, Reis RL, Khademhosseini A, Marques AP, Gomes ME. The osteogenic differentiation of SSEA-4 sub-population of human adipose derived stem cells using silicate nanoplatelets. Biomaterials 2014;35:9087-99.

[112] Murphy SV, Atala A. 3D bioprinting of tissues and organs. Nature Biotechnology 2014;32:773-85.

[113] Kozlov PV, Burdygina GI. The structure and properties of solid gelatin and the

principles of their modification. Polymer 1983;24:651-66.

[114] Sachar A, Strom TA, Serrano MJ, Benson MD, Opperman LA, Svoboda KK, et al. Osteoblasts responses to three-dimensional nanofibrous gelatin scaffolds. Journal of Biomedical Materials Research Part A 2012;100:3029-41.

[115] Wischke C, Borchert HH. Fluorescein isothiocyanate labelled bovine serum albumin (FITC-BSA) as a model protein drug: opportunities and drawbacks. Die Pharmazie 2006;61:770-4.

[116] Wang Y, Yan L, Li B, Qi Y, Xie Z, Jing X, et al. Protein-resistant biodegradable amphiphilic graft copolymer vesicles as protein carriers. Macromolecular Bioscience 2015;15:1304-13.

[117] Ma C, Jing Y, Sun H, Liu X. Hierarchical nanofibrous microspheres with controlled growth factor delivery for bone regeneration. Advanced Healthcare Materials 2015;4:2699-708.

[118] Boomer L, Liu Y, Mahler N, Johnson J, Zak K, Nelson T, et al. Scaffolding for challenging environments: materials selection for tissue engineered intestine. Journal of Biomedical Materials Research Part A 2014;102:3795-802.

[119] Hutson CB, Nichol JW, Aubin H, Bae H, Yamanlar S, Al-Haque S, et al. Synthesis and characterization of tunable poly(ethylene glycol): gelatin methacrylate composite hydrogels. Tissue Engineering Part A 2011;17:1713-23.

[120] Kim P, Yuan A, Nam KH, Jiao A, Kim DH. Fabrication of poly(ethylene glycol): gelatin methacrylate composite nanostructures with tunable stiffness and degradation for vascular tissue engineering. Biofabrication 2014;6:024112.

[121] Benton JA, DeForest CA, Vivekanandan V, Anseth KS. Photocrosslinking of gelatin macromers to synthesize porous hydrogels that promote valvular interstitial cell function. Tissue Engineering Part A 2009;15:3221-30.

[122] Head DL, Yankeelov JA, Jr. The effect of calcium chloride on the activity and inhibition of bacterial collagenase. International Journal of Peptide and Protein Research 1976;8:155-65.

[123] Moore S, Stein WH. Photometric ninhydrin method for use in the chromatography of amino acids. The Journal of Biological Chemistry 1948;176:367-88.

[124] Thomas PC, Cipriano BH, Raghavan SR. Nanoparticle-crosslinked hydrogels as a class of efficient materials for separation and ion exchange. Soft Matter 2011;7:8192-7.

[125] Odatsu T, Azimaie T, Velten MF, Vu M, Lyles MB, Kim HK, et al. Human

periosteum cell osteogenic differentiation enhanced by ionic silicon release from porous amorphous silica fibrous scaffolds. Journal of Biomedical Materials Research Part A 2015;103:2797-806.

[126] Mladenovska K, Kumbaradzi E, Dodov G, Makraduli L, Goracinova K. Biodegradation and drug release studies of BSA loaded gelatin microspheres. International Journal of Pharmaceutics 2002;242:247-9.

[127] Li P, Kim NH, Siddaramaiah, Lee JH. Swelling behavior of polyacrylamide/laponite clay nanocomposite hydrogels: pH-sensitive property. Composites Part B: Engineering 2009;40:275-83.

[128] Wahl LM, Mergenhagen SE. Regulation of monocyte/ macrophage collagenase. Journal of Oral Pathology & Medicine 1988;17:452-5.

[129] Benton JA, DeForest CA, Vivekanandan V, Anseth KS. Photocrosslinking of gelatin macromers to synthesize porous hydrogels that promote valvular interstitial cell function. Tissue Engineering: Part A 2009;15:10.

[130] Gaharwar AK, Schexnailder PJ, Kline BP, Schmidt G. Assessment of using laponite cross-linked poly(ethylene oxide) for controlled cell adhesion and mineralization. Acta Biomater 2011;7:568-77.

[131] Zhuang H, Zheng JP, Gao H, De Yao K. In vitro biodegradation and biocompatibility of gelatin/montmorillonite-chitosan intercalated nanocomposite. Journal of Materials Science Materials in Medicine 2007;18:951-7.

[132] Ball MD, Bonzani IC, Bovis MJ, Williams A, Stevens MM. Human periosteum is a source of cells for orthopaedic tissue engineering: a pilot study. Clinical Orthopaedics and Related Research 2011;469:3085-93.

[133] Ng AM, Saim AB, Tan KK, Tan GH, Mokhtar SA, Rose IM, et al. Comparison of bioengineered human bone construct from four sources of osteogenic cells. Journal of Orthopaedic Science : Official Journal of the Japanese Orthopaedic Association 2005;10:192-9.

[134] Nakahara H, Dennis JE, Bruder SP, Haynesworth SE, Lennon DP, Caplan AI. In vitro differentiation of bone and hypertrophic cartilage from periosteal-derived cells. Experimental Cell Research 1991;195:492-503.

[135] Nakahara H, Watanabe K, Sugrue SP, Olsen BR, Caplan AI. Temporal and spatial distribution of type XII collagen in high cell density culture of periosteal-derived cells. Developmental Biology 1990;142:481-5.

[136] Chang H, Knothe Tate ML. Concise review: the periosteum: tapping into a

reservoir of clinically useful progenitor cells. Stem Cells Translational Medicine 2012;1:480-91.

[137] Justesen J, Stenderup K, Eriksen EF, Kassem M. Maintenance of osteoblastic and adipocytic differentiation potential with age and osteoporosis in human marrow stromal cell cultures. Calcified Tissue International 2002;71:36-44.

[138] Shimizu T, Sasano Y, Nakajo S, Kagayama M, Shimauchi H. Osteoblastic differentiation of periosteum-derived cells is promoted by the physical contact with the bone matrix in vivo. The Anatomical Record 2001;264:72-81.

[139] Kim HK, Oxendine I, Kamiya N. High-concentration of BMP2 reduces cell proliferation and increases apoptosis via DKK1 and SOST in human primary periosteal cells. Bone 2013;54:141-50.

[140] Lebaron P, Joux F. Flow cytometric analysis of the cellular DNA content of Salmonella typhimurium and Alteromonas haloplanktis during starvation and recovery in seawater. Applied and Environmental Microbiology 1994;60:4345-50.

[141] Downs TR, Wilfinger WW. Fluorometric quantification of DNA in cells and tissue. Analytical Biochemistry 1983;131:538-47.

[142] Huang ZJ, Haugland RP, You WM, Haugland RP. Phallotoxin and actin binding assay by fluorescence enhancement. Analytical Biochemistry 1992;200:199-204.

[143] Sachar A, Strom TA, San Miguel S, Serrano MJ, Svoboda KK, Liu X. Cell-matrix and cell-cell interactions of human gingival fibroblasts on three-dimensional nanofibrous gelatin scaffolds. Journal of Tissue Engineering and Regenerative Medicine 2014;8:862-73.